



# Novel synthesis, DFT and investigation of the optical and electrical properties of carboxymethyl cellulose/thiobarbituric acid/copper oxide [CMC + TBA/CuO]<sup>C</sup> nanocomposite film

Samia M. Ibrahim<sup>1</sup> · Aymen Bourezgui<sup>2</sup> · Ahmed F. Al-Hossainy<sup>1,3</sup>

Published online: 13 August 2020

© The Polymer Society, Taipei 2020

## Abstract

A novel synthesis blend of sodium carboxymethyl cellulose (CMC) with thiobarbituric acid (TBA) [CMC + TBA]<sup>B</sup> has been doped with CuO to study the optical and direct electrical (DC) properties of [CMC + TBA/CuO]<sup>C</sup> nanocomposite films. Different characterization techniques for [CMC]<sup>TF</sup>, [TBA]<sup>TF</sup>, [CMC + TBA]<sup>B</sup> and [CMC + TBA/CuO]<sup>C</sup> such as Fourier-transform infrared spectroscopy (FTIR), Ultraviolet–visible spectroscopy (UV-Vis), X-ray diffraction (XRD), Scanning electron microscopy (SEM) and optical properties have been used. SEM showed a good dispersion of copper oxide nanoparticles [CuO]<sup>NPs</sup> on [CMC + TBA]<sup>B</sup> film surface. The dielectric constant  $\epsilon(\omega)$ , optical conductivity  $\sigma(\omega)$  and DC properties increased and demonstrated wave-like performance with increasing [CuO]<sup>NPs</sup> ratio at  $h\nu$  range of 0.7 eV – 5.0 eV. Copper content [CuO]<sup>NPs</sup> increases lead to the formation of a wide variety of 3D-semiconductor networks within [CMC + TBA]<sup>B</sup> film matrix which increase optical conductivity. The optimization was performed using density functional theory (DFT) by *DMol<sup>3</sup>* and Cambridge Serial Total Energy Package (*CASTEP*). In Experimental section by using Tauc's equation, the results clearly show that the values of optical energy band gap  $E_g^{Opt}$  decreases from 2.978 eV for [CMC]<sup>TF</sup>, 2.725 eV for [TBA]<sup>TF</sup>, 2.625 eV for [CMC + TBA]<sup>B</sup> to 2.488 eV for [CMC + TBA/CuO]<sup>C</sup>. The simulated FTIR, XRD, and optical properties by *Gaussian software* and *CATSTEP* are in great agreement with the experimental study. The [CMC + TBA/CuO]<sup>C</sup> presents a good candidate for optoelectronics and solar cell applications.

**Electronic supplementary material** The online version of this article (<https://doi.org/10.1007/s10965-020-02235-w>) contains supplementary material, which is available to authorized users.

## Highlights

- 1- Novel synthesis of [CMC + TBA]<sup>B</sup> and [CMC + TBA/CuO]<sup>C</sup> nanocomposite film.
- 2- Fabrication of nanostructure thin film of [CMC]<sup>TF</sup> and [ZnCMC]<sup>TF</sup> powder used spin coating technique of thickness  $150 \pm 2$  nm.
- 3- Characterization of [CuO]<sup>NPs</sup>, [CMC + TBA]<sup>B</sup> and [CMC + TBA/CuO]<sup>C</sup> nanocomposite film by using Fourier transform infrared spectroscopy (FT-IR), X-ray diffraction (XRD), thermal analysis (ATG), Scanning Electron Microscopy (SEM), DFT simulation, AFM spectroscopy, optical and electrical properties.
- 4- The obtained average optical energy gaps for [CMC + TBA]<sup>B</sup> and [CMC + TBA/CuO]<sup>C</sup> nanocomposite films are 2.79 eV and 2.03 eV, respectively.

✉ Ahmed F. Al-Hossainy  
ahmed73chem@scinv.au.edu.eg

<sup>1</sup> Chemistry Department, Faculty of Science, New Valley University, 72511 Al-Wadi Al-Gadid, Al-Kharga, Egypt

<sup>2</sup> Nanomaterials and Systems for Renewable Energy Laboratory, Technoparc Borj Cedria, BP 095 Hammam Lif, Tunisia

<sup>3</sup> Chemistry Department, Faculty of Science, Northern Border University, Arar 1321, Saudi Arabia

**Keywords** Copper oxide · Band gap. [CMC + TBA/CuO]<sup>C</sup> · Nanocomposite · Optical and DC properties

## Introduction

The creation and analysis of various polymer blends has been a significant focus of attention in recent years. Blending two or more polymers helps to increase the polymeric materials efficiency [1, 2]. In contrast with pure polymers or their conventional composites the mechanical, thermal and optical properties of polymers or blends with nanosized fillers have significantly improved. Moreover, the enhancement of the electric and magnetic properties of polymeric materials attracts other researchers [3, 4]. Carboxymethyl cellulose (CMC) is a smart water-soluble polyelectrolyte derivative with excellent recording and thermal gelatinization properties [5, 6]. Specific CMCs provide high viscosity, biocompatibility, biodegradability and transparency non-toxicity. It is used in many fields, such as the supply of drugs, silk prints and the paper manufacturing [7, 8]. Thiobarbituric acid (TBA) is an organic semicrystalline heterocycle, reagent for the processing of malondialdehyde, Kodak Fogging Developer (FD-70) and a member of the Kodak DPF production system that is designed

to create black and white slides. The hydrophilicity of the composite film industry is an asset for its applications [9]. TBA has strong dimensional consistency and UV visible light irradiation is photo stable. It also has a low level of oxygen permeability due to the great inter-cohesive energy produced by the strongly polar alcohol ( $-OH$ ) group (Enol form) [10, 11]. As a medium of removal of pigment, [PVA + Polyethylene (PEO) + CMC]<sup>B</sup> blends and (CMC + TBA)<sup>B</sup> blend have been used for a broad variety of applications in medicinal matter and farming [12, 13]. [CMC + PVA]<sup>B</sup> is also flexible semi-transparent and allows for healing monitoring so that it can be used as clothing replacement [14]. Specific transition metal nanoparticles have shown their effects on physical and chemical properties CMC blends. Such nanoparticles are zinc oxide nanoparticles [ZnO]<sup>NPs</sup> [15], nanoparticles of zirconium oxide [ZrO<sub>2</sub>]<sup>NPs</sup> [16] and nanoparticles of cobalt oxide [Co<sub>3</sub>O<sub>4</sub>]<sup>NPs</sup> [17]. [Graphene (GO) + CMC]<sup>C</sup> alginate composite with improved strength of tensile which was prepared by Yadva et al. [18] and Zhan et al. [19]. The blend resistivity decreased after doping 5% carbon nanotubes (CNT)/ [SiO<sub>2</sub>]<sup>NPs</sup> hybrid content from  $6 \times 10^5$  to  $3.4 \times 10^3 \Omega \cdot M$  [20]. It has been shown recently to enable practical applications in lithium ion battery doping of titanium dioxide anatase grade (TiO<sub>2</sub>) with [PVA + chitosan (CN)/lithium perlorate (LiClO<sub>4</sub>)]<sup>B</sup> blend, because it facilitates the transfer of lithium ions in the polymer matrix [21]. Copper oxide nanoparticle [CuO]<sup>NPs</sup> is an environmentally friendly and a significant antiferromagnetic p-type semiconductor [22]. [CuO]<sup>NPs</sup> has been extensively studied as a lithium ion battery electrode for pseudo-modes, ceramic pigments, and magnetic materials [23]. [CuO]<sup>NPs</sup> were prepared via several methods including the thermal decomposition and sol–gel techniques [24].

Previous studies have neglected to consider the effects of adding TBA and [CuO]<sup>NPs</sup> on the spectroscopic, thermal, and DC conductivity properties of CMC. In the present study, [CuO]<sup>NPs</sup>, [CMC + TBA]<sup>B</sup> and [CMC + TBA/CuO]<sup>C</sup> nanocomposite films were fabricated utilizing a free sol–gel process and solution casting technique, respectively. In comparison studies between experimental and simulated DFT, the structural characterization of [CuO]<sup>NPs</sup>, [CMC + TBA]<sup>B</sup> and [CMC + TBA/CuO]<sup>C</sup> were studied using characterization techniques comprising Fourier transform infrared (FTIR), thermal analysis (TGA), X-ray diffraction (XRD) and SEM spectroscopy. The optical properties, optical constants, DFT and DC properties of the novel fabricated [CMC + TBA]<sup>B</sup> and [CMC + TBA/CuO]<sup>C</sup> nanocomposite films were determined.

## Experimental details

### Materials and preparation

To synthesize [CuO]<sup>NPs</sup>, the first solution (0.1 M) was formed by dissolving 24.16 g of copper (II) nitrate [Cu(NO<sub>3</sub>)<sub>2</sub>·3H<sub>2</sub>O,

MW = 241.60, Sigma and Aldrich] in 100 ml deionized water under a magnetic stirring. The second solution (1.5 M) was formed by dissolving 18.91 g of oxalic acid [C<sub>2</sub>H<sub>2</sub>O<sub>4</sub>·2H<sub>2</sub>O, MW = 126.07, Sigma and Aldrich] in 100 ml deionized water. At temperature 50 °C with stirring continued for 2 h, the oxalic acid solution was added into the Cu(NO<sub>3</sub>)<sub>2</sub>·3H<sub>2</sub>O solution and then leave in mother 10 h at room temperature (RT). To obtain the gelatinous copper hydroxide nanoparticles, the mixed solution was stirred at 80 °C for 30 min. Finally, the obtained [CuO]<sup>NPs</sup> was calcined at 500 °C for 2 h in an air furnace.

Three CMC (20%) + TBA (80%) films were formed as follows: 1.44 g TBA [In our Lab. New Valley University, Egypt, average MW (average) = 144] was dissolved in 75 ml ionized water under 85 °C with stirring continued for 2 h till the complete dissolution of TBA. At 50 °C with stirring continued for 2 h, 0.5 g Na-CMC [Pharmaceutical Chemicals Co., Egypt] was dissolved in 25 ml ionized water, and then mixed with the TBA solution. The obtained [CMC + TBA]<sup>B</sup> solutions kept pure, and the other gelatinous solution were doped with the sol–gel prepared [CuO]<sup>NPs</sup> at ratios W = 0.3, 0.6, and 0.9% wt. utilizing the equation:  $W(\text{wt.}\%) = \left[ \frac{w_{CuO}}{w_b + w_{CuO}} \right] \times 100$ , where  $w_{CuO}$  and  $w_b$  represent the weights of [CuO]<sup>NPs</sup> and the blend of [CMC + TBA]<sup>B</sup>, respectively. In desiccator at 60 °C for 24 h, the [CMC + TBA]<sup>B</sup> solutions cast into cleaned glass petri dishes. The films were pelleted out of the petri dish and careful to produce sufficiently [CMC + TBA/CuO]<sup>C</sup> nanocomposite films. In order to prevent moisture effect nanocomposite, the fabricated [CuO]<sup>NPs</sup>, [CMC + TBA]<sup>B</sup> and [CMC + TBA/CuO]<sup>C</sup> nanocomposite films is kept in the desiccator Fig. 1.

### Characterization

Characterization methods and typical conditions are listed in Table 1.

## Results and discussions

The preparation of carboxymethyl cellulose (CMC) and thio-barbituric acid (TBA) blend [CMC + TBA]<sup>B</sup> and nanocomposite of CMC, TBA and CuO nanoparticles [CMC + TBA/CuO]<sup>C</sup> is described in the experimental section. All these bland and nanocomposite (ratios W = 0.3, 0.6, and 0.9% wt) are powder-like and partial stable in normal condition. They are readily soluble in DMF and DMSO by heating. The optical conductivity measurements of thin films suggest the optoelectronic devices and solar cell nature of the [CMC + TBA]<sup>B</sup> and [CMC + TBA/CuO]<sup>C</sup>.

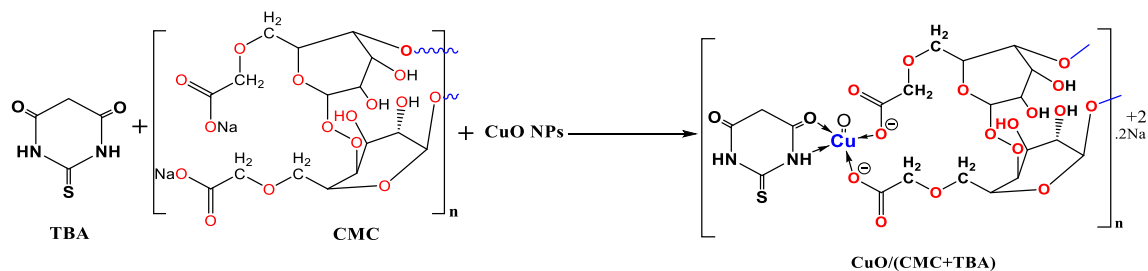


**Fig. 1** Schematic mechanism for synthesis of  $[\text{CMC} + \text{TBA}/\text{CuO}]^c$  nanocomposite film

### Fourier transform infrared spectroscopy (FTIR)

Some vibrational spectroscopic data of CMC and TBA compounds have been reported previously in the experimental and simulation IR spectrum of TBA and CMC, respectively, Fig. 1S, Fig. 2S [25]. In the experimental spectrum (Fig. 2a) for  $[\text{CMC} + \text{TBA}]^B$  and  $[\text{CMC} + \text{TBA}/\text{CuO}]^C$  thin films, a strong absorption band was detected at range  $2962\text{--}3796\text{ cm}^{-1}$  which can be attributed to intra- water molecular vibration ( $\nu_{\text{OH}}$ ) for all  $[\text{CMC} + \text{TBA}]^B$  and  $[\text{CMC} + \text{TBA}/\text{CuO}]^C$  thin films [26]. Peaks at range  $1750\text{--}1550\text{ cm}^{-1}$  was allocated to C-H bond stretching and bending vibrations ( $\nu_{\text{CH}}$  and  $\delta_{\text{CH}}$ ) for  $[\text{CMC} + \text{TBA}]^B$  and  $[\text{CMC} + \text{TBA}/\text{CuO}]^C$  thin films [27]. In contrast, the absorption bands appear at  $1300\text{ cm}^{-1}$ ,  $1351\text{ cm}^{-1}$  and  $1399\text{ cm}^{-1}$  is attributed to antisymmetric ( $\nu_{\text{CO}^-}$ ) for  $[\text{CMC} + \text{TBA}]^B$ . Also, the  $1302\text{ cm}^{-1}$ ,  $1389\text{ cm}^{-1}$  and  $1450\text{ cm}^{-1}$  bands are due to antisymmetric ( $\nu_{\text{CO}^-}$ ) for  $[\text{CMC} + \text{TBA}/\text{CuO}]^C$  thin films. Moreover, the bending vibration of the ether (glyosidic) linkage ( $\delta_{\text{C-O-O-C}}$ ) was designated by a strong peak at  $1141\text{ cm}^{-1}$  and  $1113\text{ cm}^{-1}$  for both  $[\text{CMC} + \text{TBA}]^B$  and  $[\text{CMC} + \text{TBA}/\text{CuO}]^C$  thin films, respectively [28]. The  $[\text{CMC} + \text{TBA}/\text{CuO}]^C$  thin film spectrum presents besides the in above bonds a peak that are not found in that of  $[\text{CMC} + \text{TBA}]^B$  thin film, particularly at  $526\text{ cm}^{-1}$  and  $471\text{ cm}^{-1}$  which are allocated to  $\text{CuO} \rightarrow \text{O}$  rocking of  $[\text{CMC} + \text{TBA}/\text{CuO}]^C$  thin films. The spectrum of the  $[\text{CuO}]^{\text{NPs}}$  thin films exhibit additional FTIR strong broad band at near  $471\text{ cm}^{-1}$  assigned to  $\nu(\text{Cu-O})$  modes [29, 30].

The results of the TD-DFT simulations are similar to the experimental absorption and emission data for  $[\text{CMC} + \text{TBA}]^B$  and  $[\text{CMC} + \text{TBA}/\text{CuO}]^C$  demonstrated in Fig. 2b and c. Numerous spectroscopic analyses of blends and composites using both solution and solid matrix absorption and luminescence methods have been performed [31]. The focus in our comparison will be on the peak's intensity and location on wavenumber states within  $0\text{ cm}^{-1} \leq \text{Wavenumber} \leq 3750\text{ cm}^{-1}$  of the onset of absorption or emission. The computed parameters at the  $[\text{CMC} + \text{TBA}]^B$  and  $[\text{CMC} + \text{TBA}/\text{CuO}]^C$  are also given for the sake of comparison [32]. In order to compare all methods used, it is preferable to calculate the mean location of wavenumber with transmittance %. The mean location of wavenumber for the bending and stretching vibration of  $[\text{CMC} + \text{TBA}]^B$  and  $[\text{CMC} + \text{TBA}/\text{CuO}]^C$  in experiential resulted are good agreement with the *Gaussian9/DFT/WB97XD* calculations [33]. Finally, it is noticed that, the results from the experimental method and *Gaussian* computation of the IR spectra bands for  $[\text{CMC} + \text{TBA}]^B$  and  $[\text{CMC} + \text{TBA}/\text{CuO}]^C$  show at the same wavenumber in Fig. 2a-c.

### Thermal analysis

The thermogram spectrum (TGA and DrTGA), illustrated in Fig. 3, shows that the major loss of weight starts at  $32.11\text{ }^\circ\text{C}$  for  $[\text{CMC} + \text{TBA}]^B$  and  $[\text{CMC} + \text{TBA}/\text{CuO}]^C$ . Weight loss in the first stage starts at  $56.88\text{ }^\circ\text{C}$ , this step

**Table 1** Characterization methods, model and specifications for the fabricated  $[\text{CuO}]^{\text{NPs}}$ ,  $[\text{CMC} + \text{TBA}]^B$  and  $[\text{CMC} + \text{TBA}/\text{CuO}]^C$  nanocomposite films

Characterization method	Model used and specifications
FT-IR	Perkin-Elmer FT-IR type 1650 spectrophotometer (wavelength range $4000\text{--}200\text{ cm}^{-1}$ ).
TGA	Perkin Elmer Thermogravimetric Analyzer TGA 4000 was employed. Temperature range $50\text{--}995\text{ }^\circ\text{C}$ and heating rate is $10\text{ }^\circ\text{C}/\text{min}$ in nitrogen atmosphere.
XRD	Philips X-ray diffractometer (model X'pert) with mono-chromatic Cu $K\alpha$ radiation operated at $40\text{ kV}$ and $25\text{ mA}$ .
SEM	Scanning electron microscopy (SEM; Inspect S, FEI, Holland), operated at an accelerating voltage of $3.0\text{ kV}$
Film thickness and rate monitor	Model FTM4. Edwards, England ( $150 \pm 2\text{ nm}$ )
UV	SHIMADZU UV-3101 UV-Vis-NIR pc.

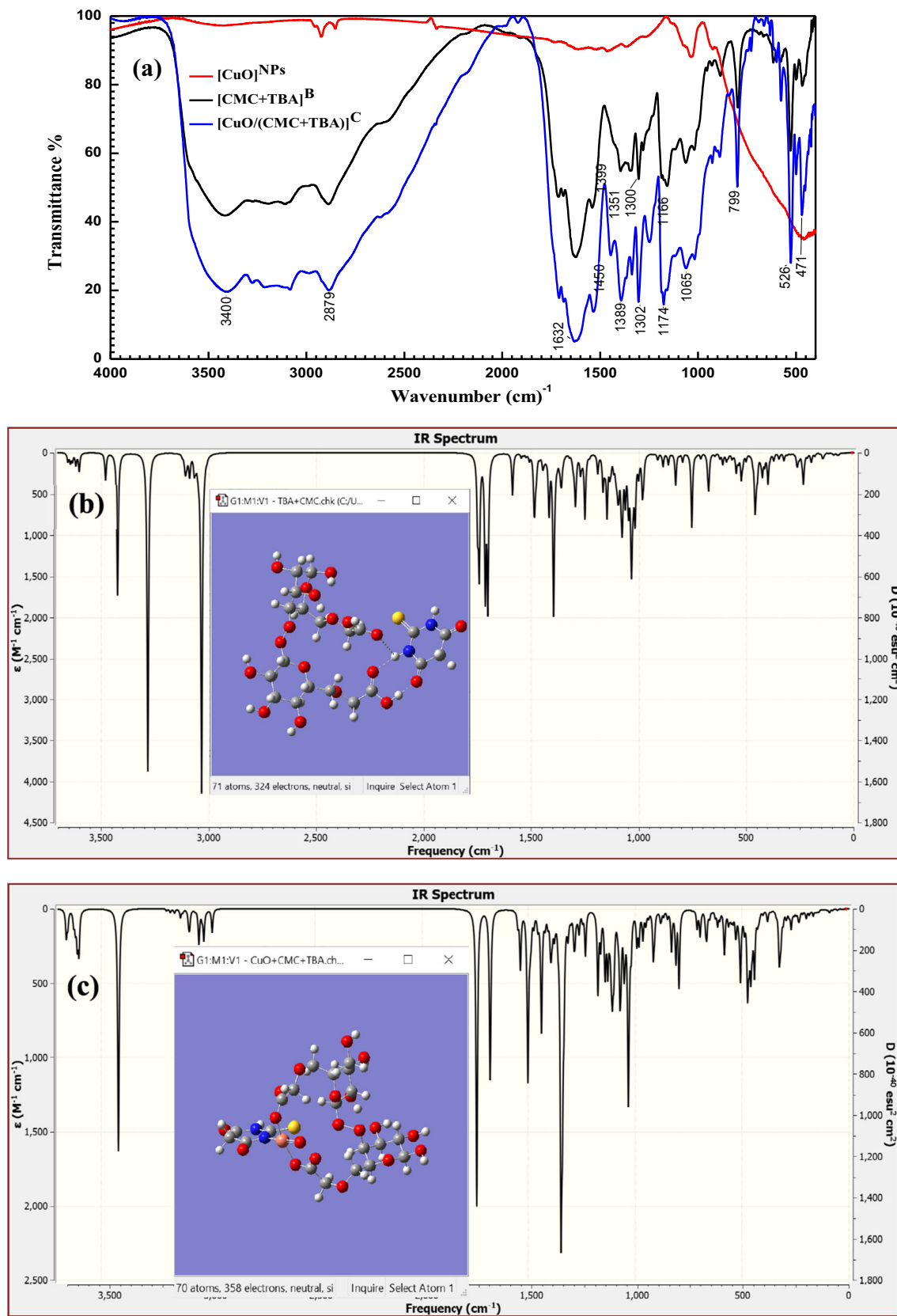
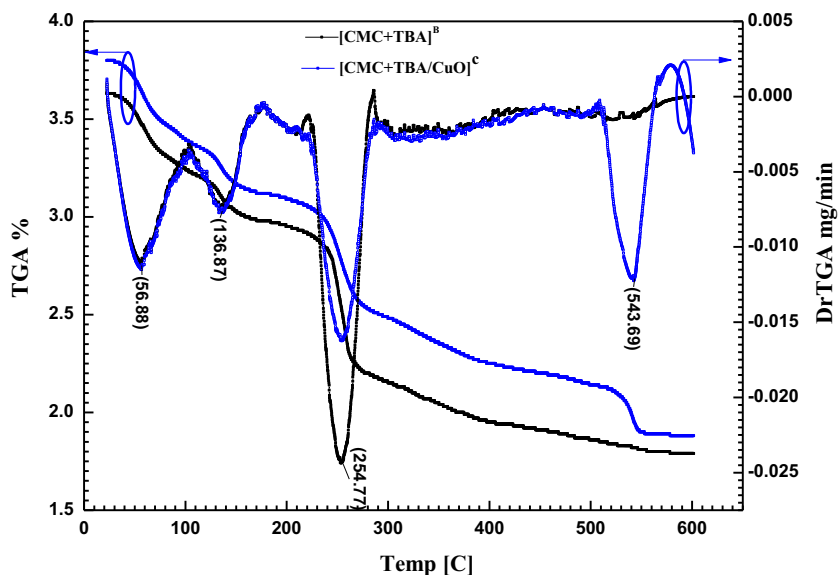


**Fig. 2** a FTIR spectrum of CuO<sup>NPs</sup>, [CMC + TBA]<sup>B</sup> and [CMC] + TBA/CuO<sup>C</sup>; b IR spectrum of [CMC + TBA]<sup>B</sup> by using DFT simulation and c) IR spectrum of [CMC] + TBA/CuO<sup>C</sup> by using DFT simulation



**Fig. 3** TG and DrTGA thermogram of [CMC + TBA]<sup>B</sup> and [CMC + TBA/CuO]<sup>C</sup> as powder form



is attributed to the loss of hydrated water [34]. The second stage at 136.78 °C is due to the loss of 2NO<sub>2</sub> and O<sub>2</sub> fragments. The third loss of weight stage (254.77 °C) is attributed to sodium 2-(((2S, 3S, 4R, 5S, 6S)-3,4,5,6-tetrahydroxytetrahydro-2H-pyran-2-yl) methoxy) acetate existing in the matrix of molecule. This compound undergoes two steps of decomposition with weight loss of 62.94%. Finally, the thermographic TGA and DrTGA for [CMC + TBA/CuO]<sup>C</sup> appeared peak at 543.69 °C not appeared in [CMC + TBA]<sup>B</sup>. Thus, the last one of [CMC + TBA/CuO]<sup>C</sup> is due to loss of TBA and CMC fragments which attached with [CuO]<sup>NPs</sup> [35].

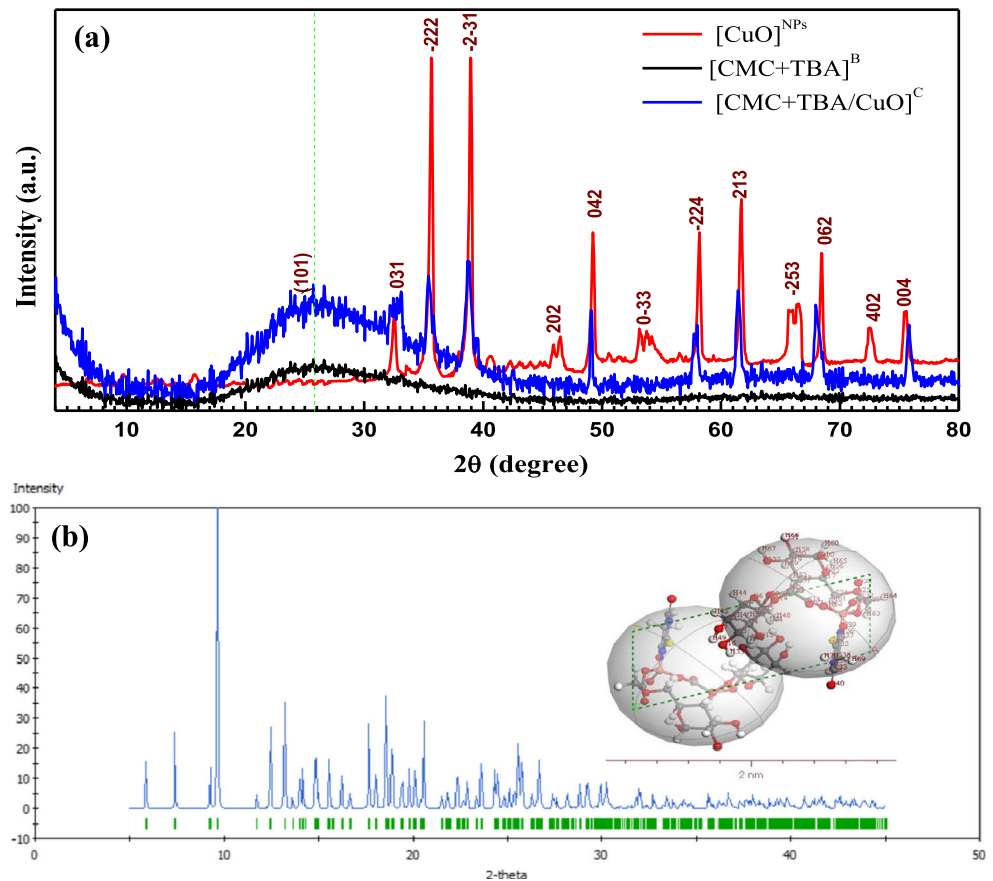
## XRD

The XRD is used to detect atomic structural properties such as grain strain length structure of phases, desired orientation, order disorder change, thermal production and the multilayer thickness. An XRD study results in a diffractogram displaying the frequency of diffractive angles (2θ) [36]. Several specific signals in 4° < 2θ < 80° domain were illustrated describing high crystallinity and good shape in the sample (Fig. 4a). In the [CMC + TBA]<sup>B</sup> thin film, the main peak located at 2θ = 25.81°, which due to (101) reflection. The d-spacing determined by XRD was 3.449 Å. The polymeric structures are also shown by the different signals and location of the Bragg peaks (2θ) [37]. In this pattern the [CuO]<sup>NPs</sup> and [CMC + TBA/CuO]<sup>C</sup> exhibit the most dignitaries signals at 031,  $\bar{2}22$ ,  $\bar{2}\bar{3}1$ , 042,  $\bar{2}24$ , 213, 062 and 004 corresponding to the crystalline nature of [CuO]<sup>NPs</sup> film. [CuO]<sup>NPs</sup> and [CMC + TBA/CuO]<sup>C</sup> diffraction from Bragg shows that the thin of nanoparticles and composite have a crystalline morphology with a triclinic system [38].

The chemical structure matrix of [CMC + TBA/CuO]<sup>C</sup> contained pyran ring (CMC molecule) as quinoid ring and pyrimidine ring (TBA molecule) as benzenoid ring. Thus, the [CMC + TBA/CuO]<sup>C</sup> crystallinity is attributed to the classification of quinoid and benzenoid rings inside [CMC + TBA]<sup>B</sup> chains. The peaks corresponding to  $hkl = \bar{2}22$  and  $\bar{2}\bar{3}1$  computed the distances of Van Der Waals between layers of phenylene rings across CMC polymer chains [39]. The [CuO]<sup>NPs</sup> and [CMC + TBA/CuO]<sup>C</sup> parameters of lattice are  $a = 7.42(3)$  Å,  $b = 9.08(2)$  Å, and  $c = 6.68(1)$  Å, while  $\alpha = 89.0(2)$ ,  $\beta = 112.8(2)$  and  $\gamma = 91.5(3)$ °. The average distance between the d-spacing atomic layers is 1.78 Å. The average crystallite size of [CuO]<sup>NPs</sup> and [CMC + TBA/CuO]<sup>C</sup> are  $D_{av} = 25.479$  nm and  $D_{av} = 28.09$  nm provided by the Table 2, respectively. At full width half-maximum intensity (FWHM), the [CuO]<sup>NPs</sup> and [CMC + TBA/CuO]<sup>C</sup> crystalline size (D) of all peaks was measured at  $4 \leq 2\theta \leq 80^\circ$ . The d-spacing of the highest crystalline signal is determined using Bragg's equation by Debye – Scherrer [40].

The diffraction line demonstrations that the values of the maximums conform with the values defined by *Crystal Sleuth Software and material studio software* [41]. The XRD structure matrix of the fabricated [CuO]<sup>NPs</sup>, [CMC + TBA]<sup>B</sup> and [CMC + TBA/CuO]<sup>C</sup> thin film referring to measurement, computed and crystal device variance, miller index (hkl), d-spacing (d), FWHM and peak strength as shown in Table 2. When comparing the results obtained from the measurement by SEM and XRD for crystallite size (D) of fabricated [CuO]<sup>NPs</sup>, [CMC + TBA]<sup>B</sup> and [CMC + TBA/CuO]<sup>C</sup> nanocomposite films, it has been found that the (D) produced by SEM is higher than that of the XRD as the figures depend on the surface of the morphology and are available in the aggregated particles. The XRD used methods to identify

**Fig. 4** **a** XRD pattern of the sol-gel prepared  $[\text{CuO}]^{\text{NPs}}$ ,  $[\text{CMC} + \text{TBA}]^{\text{B}}$  and  $[\text{CMC} + \text{TBA}/\text{CuO}]^{\text{C}}$ , **b** XRD pattern of the simulated  $[\text{CMC} + \text{TBA}/\text{CuO}]^{\text{C}}$  by using DFT



$[\text{CMC} + \text{TBA}/\text{CuO}]^{\text{C}}$  thin film crystal phases (Fig. 4a) and to check conformity with the simulation DFT spectrum. The resulted *CASTEP program in DFT calculations* methodology of  $[\text{CMC} + \text{TBA}/\text{CuO}]^{\text{C}}$  used structural properties of the simulation as ground state, as shown in Fig. 4b.

## SEM

In the novel fabricated  $[\text{CMC} + \text{TBA}/\text{CuO}]^{\text{C}}$  nanocomposite films, the distribution of  $[\text{CuO}]^{\text{NPs}}$  is shown in the Fig. 5. The surfaces of pure  $[\text{CMC} + \text{TBA}]^{\text{B}}$  blend appeared smooth in

**Table 2** XRD data of  $[\text{CuO}]^{\text{NPs}}$  and  $[\text{CMC} + \text{TBA}/\text{CuO}]^{\text{C}}$ ; crystal data,  $hkl$ , FWHM, d-spacing and D as  $2\theta$  function

Samples	$2\theta$ ( $^\circ$ )	$hkl$	FWHM	d ( $\text{\AA}$ )	D (nm)	$\text{PI}^{(\text{a})}$	FWHM	D (nm)	$\text{PI}^{(\text{b})}$
$[\text{CuO}]^{\text{NPs}}$ and $[\text{CMC} + \text{TBA}/\text{CuO}]^{\text{C}}$	32.475	031	0.3612	2.720	23.94	266	0.554	15.61	130
	35.599	$\bar{2}22$	0.2970	2.491	29.36	1453	0.3870	22.54	310
TRICLINIC [42]	38.897	$\bar{2}\bar{3}1$	0.2977	2.289	29.58	1476	0.3468	25.39	445
	46.286	202	0.8682	1.943	10.40	96	–	–	–
Cell parameters	49.189	042	0.2906	1.836	31.43	624	0.1881	48.55	515
	53.691	$0\bar{3}\bar{3}$	1.8549	1.693	5.02	119	–	–	–
$\alpha = 89.0(2)^\circ$ , $\gamma = 91.5(3)^\circ$ ; $\beta = 112.8(2)^\circ$	58.127	$\bar{2}24$	0.2865	1.575	33.16	665	0.3271	29.04	235
rmse = 0.001567 V = 410(2)	61.641	213	0.3049	1.494	31.71	869	0.3543	27.29	461
	66.107	$\bar{2}53$	1.3624	1.404	7.27	273	–	–	–
	68.420	062	0.2777	1.363	36.16	619	0.3540	28.36	306
	72.482	402	0.3324	1.296	30.97	168	–	–	–
	75.588	004	0.2859	1.257	36.75	289	0.3760	27.95	310
Average values				1.780	25.479			28.09	

$\text{PI}^{(\text{a})}$ :  $[\text{CuO}]^{\text{NPs}}$  and  $\text{PI}^{(\text{b})}$ :  $[\text{CMC} + \text{TBA}/\text{CuO}]^{\text{C}}$

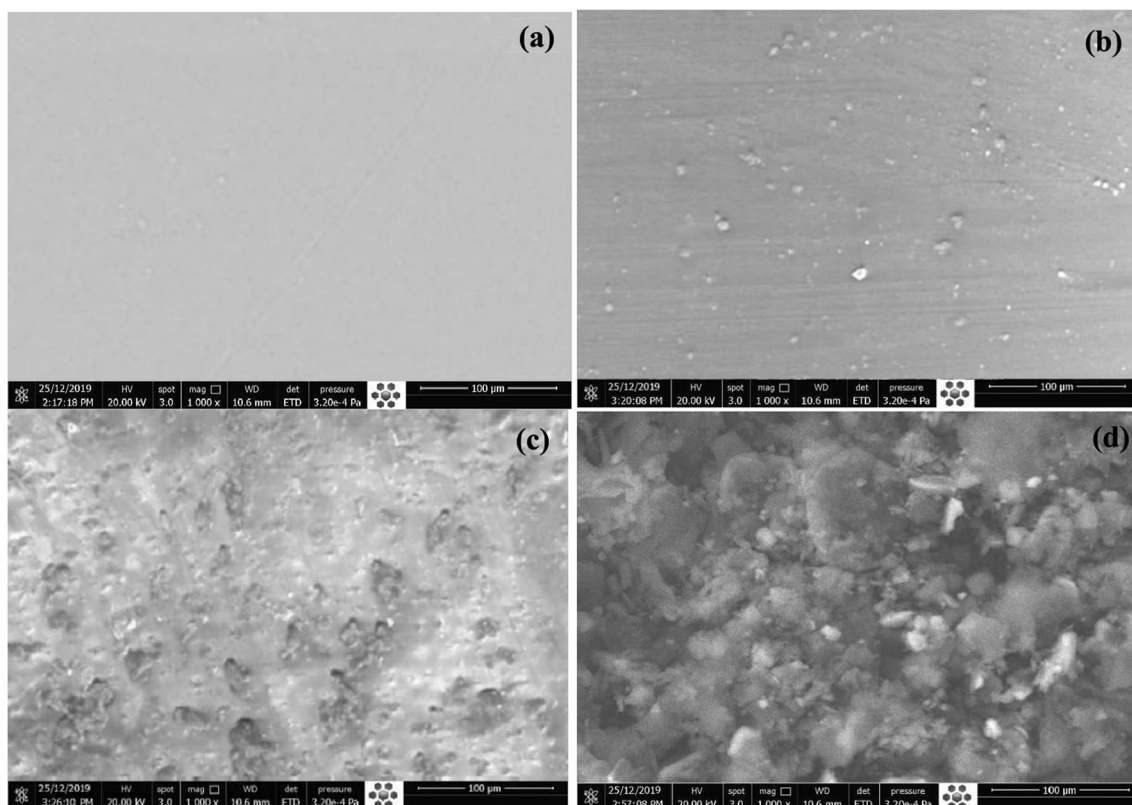


**Fig. 5** SEM for (a) pure  $[\text{CMC} + \text{TBA}]^{\text{B}}$  blend (b) 0.3 wt.% (c) 0.6 wt.% and (d) 0.9 wt.% CuO doped  $[\text{CMC} + \text{TBA}/\text{CuO}]^{\text{C}}$  thin films

Fig. 5a. Fig 5b–d demonstrate the uniform distribution of the  $[\text{CuO}]^{\text{NPs}}$ . When  $[\text{CuO}]^{\text{NPs}}$  is loaded into the  $[\text{CMC} + \text{TBA}]^{\text{B}}$  blend matrix, small holes were produced. The improvement in conductivity by increasing  $[\text{CuO}]^{\text{NPs}}$  content can be related by physical contact of  $[\text{CuO}]^{\text{NPs}}$  in the polymer matrix to the formation of linked networks [43]. These networks cannot be continuous with low  $[\text{CuO}]^{\text{NPs}}$  content. The connected network density increases with increasing  $[\text{CuO}]^{\text{NPs}}$  content and subsequently the conductivity increases.  $[\text{CuO}]^{\text{NPs}}$  on the other hand, is a semiconductor (as shown in Fig. 6) which may cause the creation of energy levels within the  $E_g$  of the fabricated  $[\text{CMC} + \text{TBA}]^{\text{B}}$  blend while combining  $[\text{CuO}]^{\text{NPs}}$  with  $[\text{CMC} + \text{TBA}]^{\text{B}}$ . Such new levels of energy serve as traps for charge carriers passing between them, leading to enhance conductivity [44, 45].

### Molecular electrostatic potential (MEP), electron density (ED) and potential (P)

The chemical and physical similarities of  $[\text{CMC} + \text{TBA}]^{\text{B}}$  and  $[\text{CMC} + \text{TBA}/\text{CuO}]^{\text{C}}$  have been investigated by utilizing the electron density and the electrostatic potential. The use of electron density as the essential factor to define the ground state of a many electron system is further discussed for  $[\text{CMC} + \text{TBA}]^{\text{B}}$  and  $[\text{CMC} + \text{TBA}/\text{CuO}]^{\text{C}}$ , respectively. The MEP has been used to describe the electrostatic potential

depending on the constant electron density surface. The active location of MEP is displayed by a 3D illustration in Fig. 6a and d for  $[\text{CMC} + \text{TBA}]^{\text{B}}$  and  $[\text{CMC} + \text{TBA}/\text{CuO}]^{\text{C}}$ , respectively. The blue color constitutes the propitious zone for the nucleophilic attack, while the propitious zone for electrophilic attacks is constituted by a red color. The potential range [P] of the matrix  $[\text{CMC} + \text{TBA}]^{\text{B}}$  and  $[\text{CMC} + \text{TBA}/\text{CuO}]^{\text{C}}$  in the isolated molecule and crystal models are  $-7.120 \times 10^{-2} \geq [P] \geq 7.120 \times 10^{-2}$  and  $-7.634 \times 10^{-2} \geq [P] \geq 7.634 \times 10^{-2}$ , respectively, while the increase follows the order: red < brown < blue [46]. The blue color is the largest attraction, whereas the red color is a powerful repudiation. The diagram of the MEP reveals that nitrogen electronegative atoms reflect the regions of negative potential and hydrogen atoms have a positive potential [47]. The potential possible diagrams (Fig. 6b and e), the potential growth of  $[\text{CMC} + \text{TBA}]^{\text{B}}$  is shown to be lower than that of  $[\text{CMC} + \text{TBA}/\text{CuO}]^{\text{C}}$ . This indicates an increased probability of electron transition in  $[\text{CMC} + \text{TBA}/\text{CuO}]^{\text{C}}$ .

### AFM of $[\text{CMC} + \text{TBA}/\text{CuO}]^{\text{C}}$ thin film

The AFM images of the novel fabricated  $[\text{CMC} + \text{TBA}/\text{CuO}]^{\text{C}}$  thin film are demonstrated in Fig. 7a–c. The surface morphology of a  $[\text{CMC} + \text{TBA}/\text{CuO}]^{\text{C}}$  thin film shows clearly the nature of the film structure from the



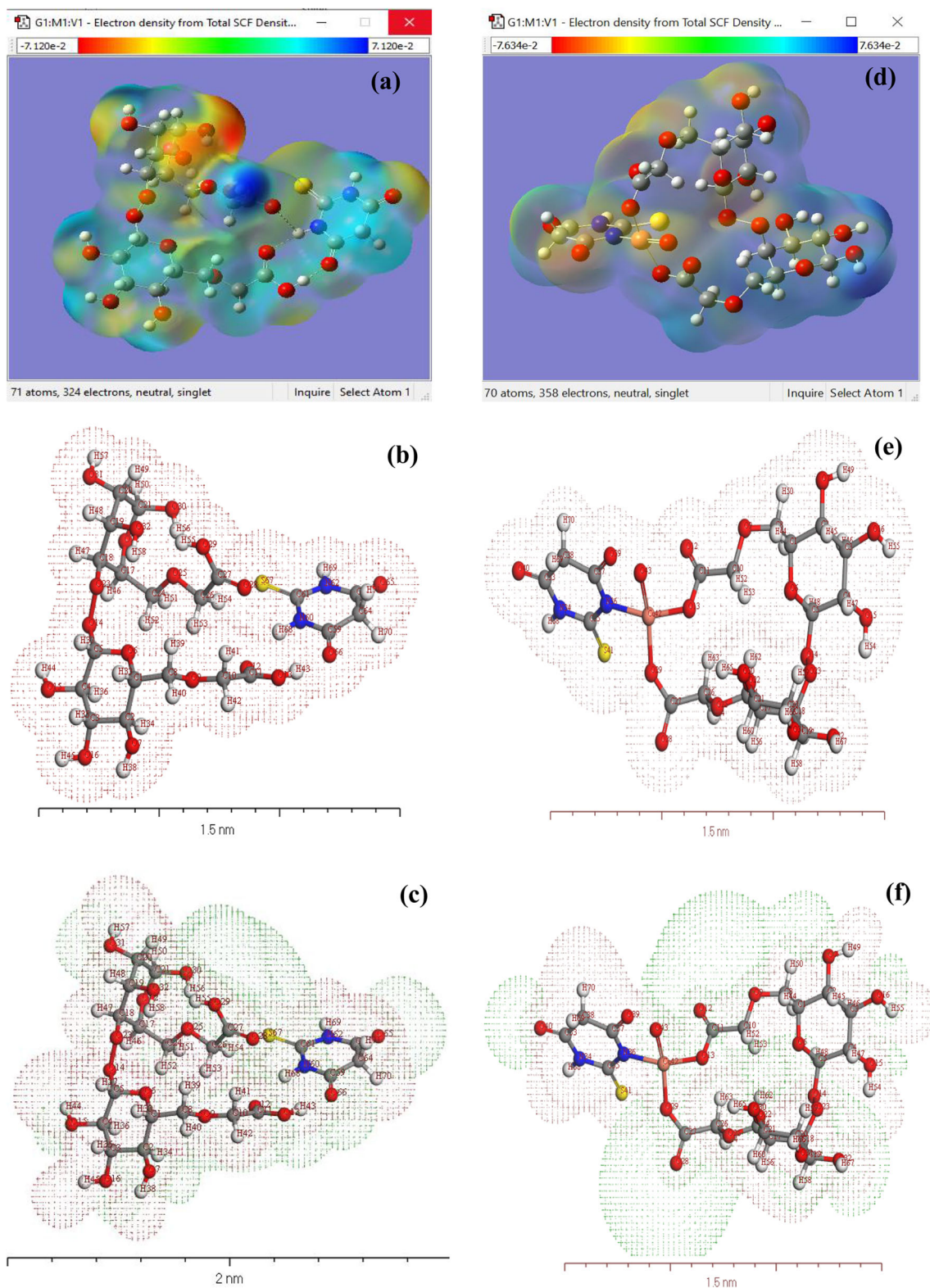


**Fig. 6** **a** MEP of  $[\text{CMC} + \text{TBA}]^{\text{B}}$ ; **b** Electron density of  $[\text{CMC} + \text{TBA}]^{\text{B}}$ ; **c** Potential of  $[\text{CMC} + \text{TBA}]^{\text{B}}$ ; **d** MEP of  $[\text{CMC} + \text{TBA}/\text{CuO}]^{\text{C}}$ ; **e** Electron density of  $[\text{CMC} + \text{TBA}/\text{CuO}]^{\text{C}}$  and **f** Potential of  $[\text{CMC} + \text{TBA}/\text{CuO}]^{\text{C}}$  by using DFT calculation in *material studio* and *Gaussian software* programs

3-dimensional AFM images. The  $[\text{CuO}]^{\text{NPs}}$  is dispersed well on the surface of the  $[\text{CMC} + \text{TBA}/\text{CuO}]^{\text{C}}$  thin film in the Fig. 7a. The surface of the fabricated  $[\text{CMC} +$

$\text{TBA}/\text{CuO}]^{\text{C}}$  thin film consists of luminous  $[\text{CuO}]^{\text{NPs}}$  allocated over all the scanned area. These luminous  $[\text{CuO}]^{\text{NPs}}$  structure transformed into randomly directed

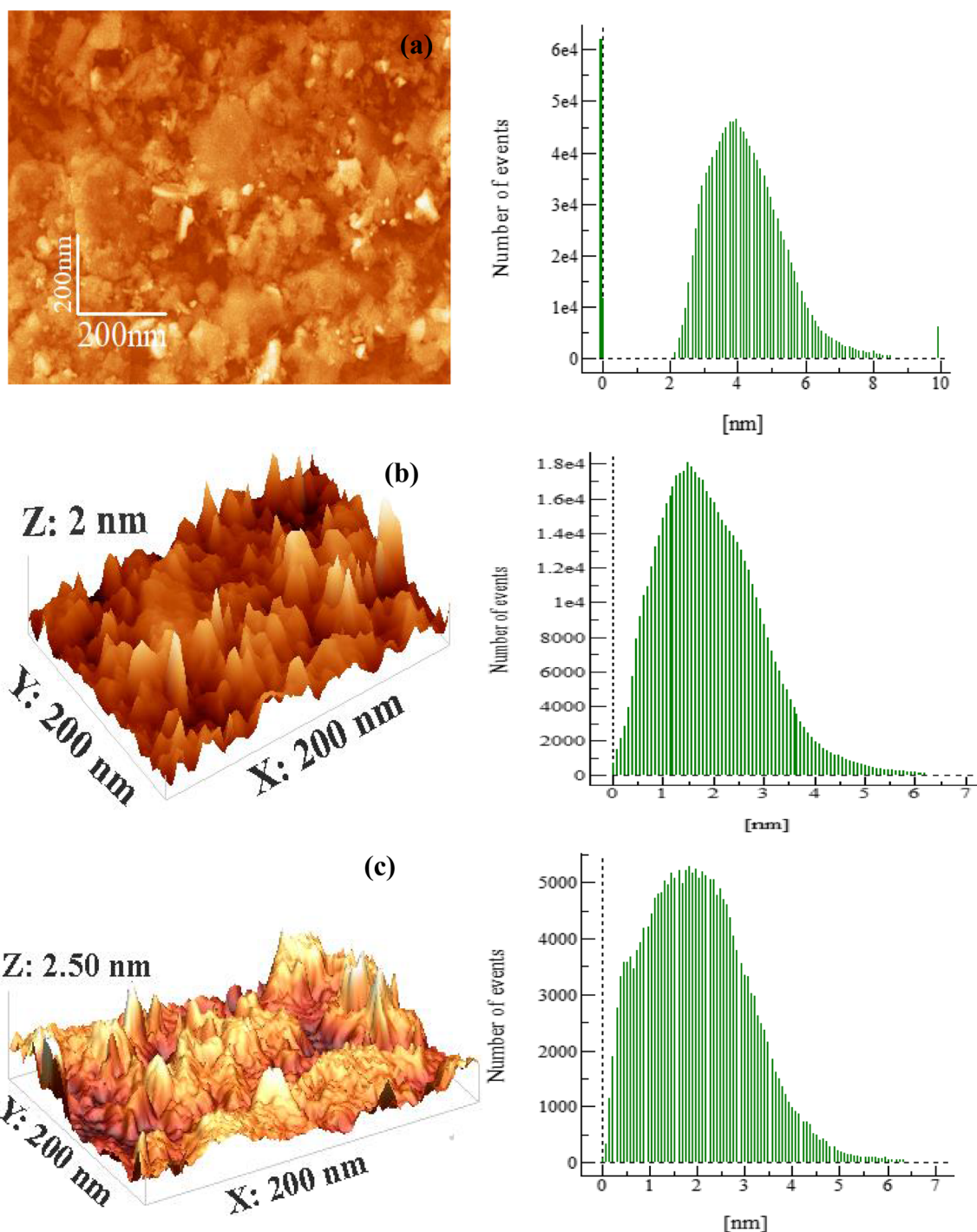
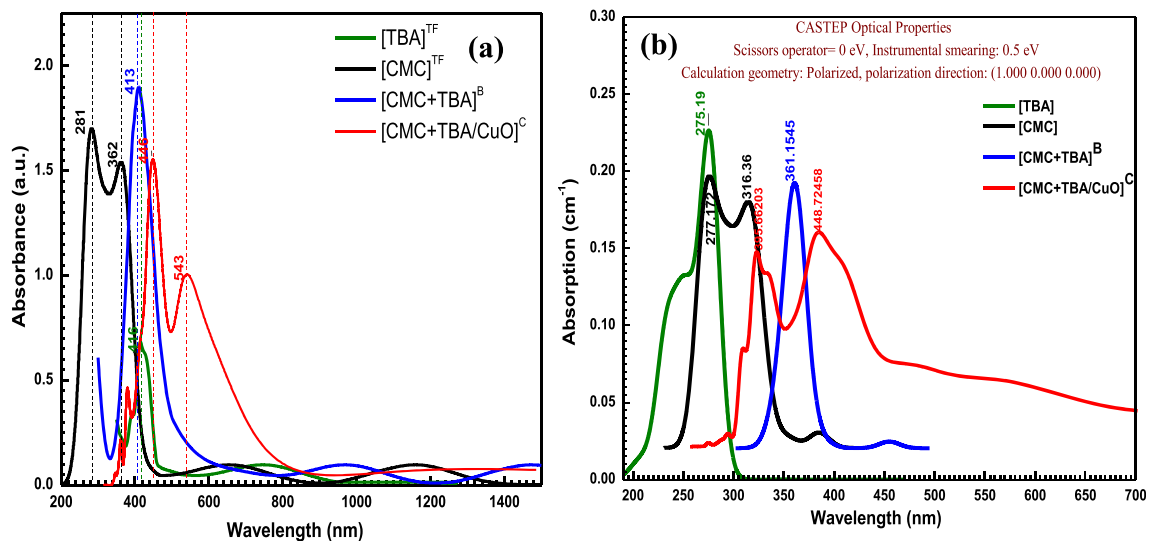


Fig. 7 AFM measurements (200 nm × 200 nm) 3D images for [CuO/(TBA + CMC)]<sup>TF</sup> blend surface

nanoparticles. In the novel fabricated [CMC + TBA/CuO]<sup>C</sup>, the roughness of the surface is described by measuring the parameters of roughness which are measured by analyzing the scans of the nanocomposite film surface. The roughness parameters were defined by using AFM to evaluate the Fig. 7b-c. These parameters are including root mean square roughness ( $R_{rms}$  =

1.0168 nm), average roughness ( $R_{av}$  = 0.8025 nm), maximum peak height ( $R_p$  = 7.1999 nm), the average height ( $d_{av}$  = 1.87 nm), surface skewness ( $Ssk$  = 0.8596 nm), and surface kurtosis ( $Sku$  = 4.3056 nm). In addition, it was found that the average crystallite size ( $D_{av}$ ) is  $\cong 52 \pm 3$  nm [48]. The surface crystallite growth and aggregation of smaller grains may be directly responsible





**Fig. 8** a Spectral dependence of the absorption for the [CMC]<sup>TF</sup>, [TBA]<sup>TF</sup>, [CMC + TBA]<sup>B</sup> and [CMC + TBA/CuO]<sup>C</sup> thin film and b) *CASTEP* program for the CMC, TBA, [CMC + TBA]<sup>B</sup> and [CMC + TBA/CuO]<sup>C</sup> as single crystal

for the highest roughness estimated value [49]. The average AFM-computed crystallite size ( $D_{av}$ ) is greater than XRD computer software and simulated *CASTEP* program in *DFT* calculations. This indicates that more than one crystallite may be from the computed AFM parameters with a grain or particle size. This proposes that more than one crystallite can be produced from measured AFM parameters that provide the grain or particle size. While, the XRD crystallite parameters depend on XRD refraction and reflection.

### Optical properties of [CMC + TBA]<sup>B</sup> and [CMC + TBA/CuO]<sup>C</sup> thin film

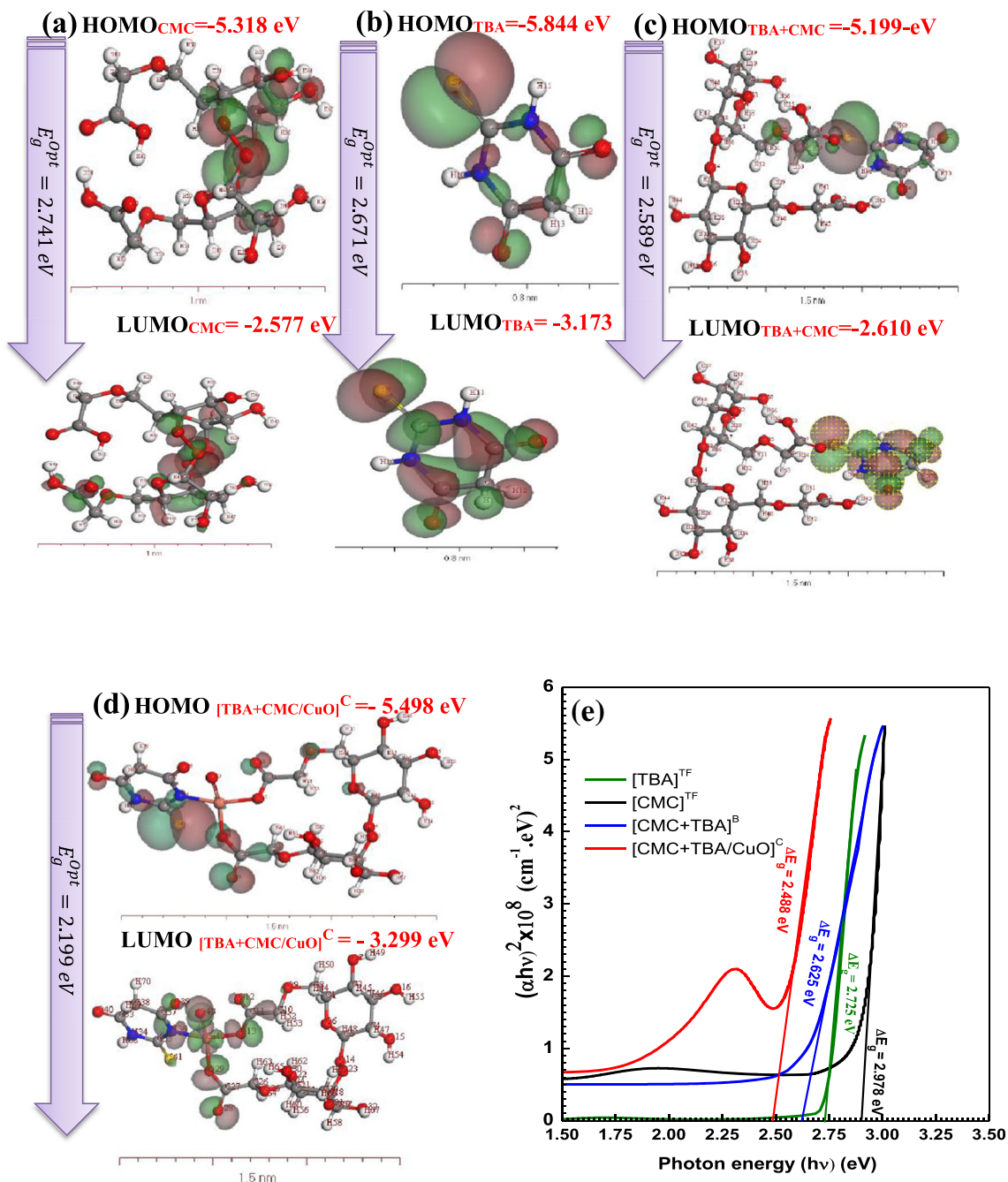
Figure 8a show the absorption spectra of [CMC]<sup>TF</sup>, [TBA]<sup>TF</sup>, [CMC + TBA]<sup>B</sup> and [CMC + TBA/CuO]<sup>C</sup> thin film, measured over the wavelength ( $\lambda$ )  $200 \leq \lambda \leq 1500$  nm. For [CMC]<sup>TF</sup>, [TBA]<sup>TF</sup>, [CMC + TBA]<sup>B</sup> and [CMC + TBA/CuO]<sup>C</sup> thin film, two absorption peaks at 281 and 362 nm, one absorption peak at 416 nm, one absorption peak at 416 nm, 413 nm and two absorption peaks at 446 and 543 nm are attributed to  $\pi \rightarrow \pi^*$  electronic transition, respectively. Moreover, the values of absorption peaks at about  $281 \leq \lambda \leq 543$  nm are due to transition of electrons from the highest occupied molecular orbital (HOMO) to the lowest unoccupied molecular orbital LUMO, which is related to  $\pi \rightarrow \pi^*$  electronic transition for [CMC]<sup>TF</sup>, [TBA]<sup>TF</sup>, [CMC + TBA]<sup>B</sup> and [CMC + TBA/CuO]<sup>C</sup> nanocomposite films [50].

Figure 8b shows the ratio of absorption Fig. 8b versus the wavelength ( $\lambda$ ) (x-axis) of the CMC, TBA, [CMC + TBA]<sup>B</sup> and [CMC + TBA/CuO]<sup>C</sup> as single crystal within a range of 200–700 nm using the *CASTEP* program in *DFT* calculations. While, the simulation curve of optical

characterization of CMC, TBA, [CMC + TBA]<sup>B</sup> and [CMC + TBA/CuO]<sup>C</sup>, there are good agreements with experimental method (Fig. 8a) in curve behavior but different in the peaks position and intensity due to the theoretical study of these compounds in single crystal and gaseous states [51].

The electronic excitation from the valence band to the conduction band induces the absorption along the fundamental absorption edges. Spectral absorption analyzes near the fundamental absorption edges are commonly unitized to deduce the optical band gap value  $E_g^{Opt}$ . The optical transitions occur by direct or indirect transitions in semiconductor materials [52]. Optical band gap  $E_g^{Opt}$  and transition band gap ( $E_g^{trans}$ ) values can be obtained by using the Tauc's equation from the optical transition spectrum  $(\alpha h\nu)^m = B(h\nu - E_g)$ , where  $h\nu$  represent the incident photons energy and  $m = 2$  for direct and 0.5 for indirect transitions allowed.

The transitions between the valence and the conduction bands are direct transitions for [CMC]<sup>TF</sup>, [TBA]<sup>TF</sup>, [CMC + TBA]<sup>B</sup> and [CMC + TBA/CuO]<sup>C</sup> thin film. The value of the optical gap energy  $E_g^{Opt}$  is obtained by extrapolating the right part of the plot  $(\alpha h\nu)^2$  as a function of  $(h\nu)$  to the energy axis at  $\alpha = 0$ . Figure 9e shows the plot of  $(\alpha h\nu)^2 \times 10^8$  (eV<sup>m</sup>)<sup>2</sup> versus photon energy  $h\nu$  (eV) [53]. The optical band gap  $E_g^{Opt}$  is defined as the lower energy value and assigned to Frankel-exciton generation, or a bound electron-hole pair.  $E_g^{Opt}$  is the energy gap with higher energy value (Also called transport gap energy) and it refers to the difference in energy value between LUMO and HOMO [54]. In Experimental section by using Tauc's equation, the results clearly show that the values of optical energy band gap  $E_g^{Opt}$  decreases from 2.978 eV for [CMC]<sup>TF</sup>, 2.725 eV for [TBA]<sup>TF</sup>, 2.625 eV for [CMC + TBA]<sup>B</sup> to 2.488 eV for [CMC + TBA/CuO]<sup>C</sup>. The



**Fig. 9** a HOMO & LUMO for the [CMC]; b HOMO & LUMO for the [TBA]; c HOMO & LUMO for the [CMC + TBA]<sup>B</sup>; d HOMO & LUMO for the [CMC + TBA/CuO]<sup>C</sup> and Experimental plot of  $(\alpha h\nu)^2$  versus photon energy (hv)

**Table 3** Calculated  $E_H$ ,  $E_L$ ,  $\mu$ ,  $\chi$ ,  $\sigma$ ,  $S$ ,  $\eta$ ,  $\omega$  and  $\Delta N_{max}$  for [CMC], [TBA], [CMC + TBA]<sup>B</sup> and [CMC + TBA/CuO]<sup>C</sup> as single crystal

Compound	$E_H$	$E_L$	$(E_H - E_L)$	$\chi$ (eV)	$\mu$ (eV)	$\eta$ (eV)	$S$ (eV)	$\omega$ (eV)	$DN_{max}$	$(eV^{-1})$
[CMC]	-5.318	-2.577	-2.741	3.9475	-3.948	1.3705	0.3648	5.6851	2.8803	0.7297
[TBA]	-5.844	-3.173	-2.671	4.5085	-4.509	1.3355	0.3744	7.6101	3.3759	0.7488
[CMC + TBA] <sup>B</sup>	-5.199	-2.61	-2.589	3.9045	-3.905	1.2945	0.3862	5.8884	3.0162	0.7725
[CMC + TBA/CuO] <sup>C</sup>	-5.498	-3.299	-2.199	4.3985	-4.399	1.0995	0.4548	8.7980	4.0005	0.9095

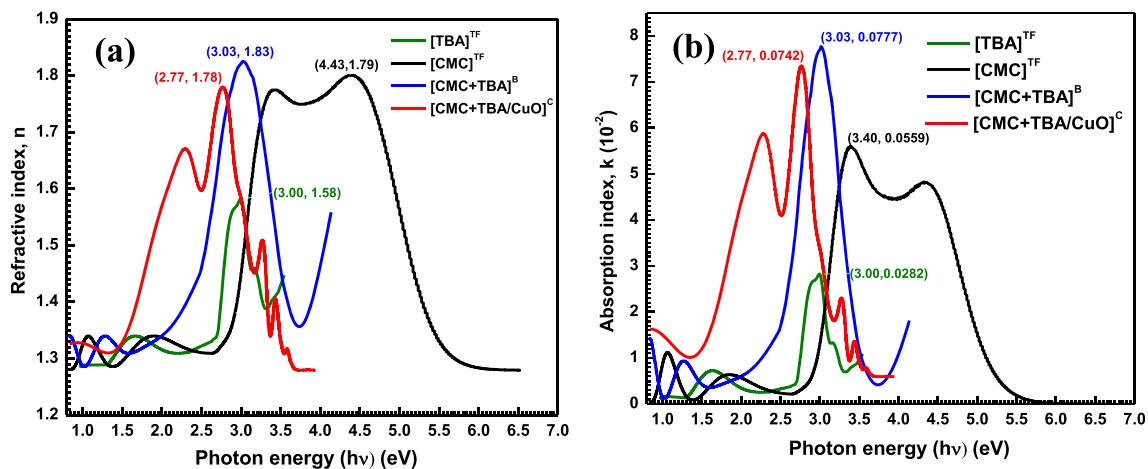


**Fig. 10** a The spectral dependence of the refractive index  $n(\lambda)$  with  $\lambda$  nm. b The absorption index  $k(\lambda)$  with  $\lambda$  nm for [CMC]<sup>TF</sup>, [TBA]<sup>TF</sup>, [CMC + TBA]<sup>B</sup> and [CMC + TBA/CuO]<sup>C</sup> as-deposited thin film

various between the  $E_g^{Opt}$  of [CMC + TBA]<sup>B</sup> to [CMC + TBA/CuO]<sup>C</sup> is 0.137 eV. This means that CuO metal introduces energy levels within the band gap which contributes to decrease the value of energy gap. In simulation section using DFT by DMol<sup>3</sup>, the  $E_g^{Opt}$  values for [CMC], [TBA], [CMC + TBA]<sup>B</sup> and [CMC + TBA/CuO]<sup>C</sup> are 2.741 eV; 2.671; 2.589 and 2.199 eV, respectively [55]. It is also important to note that, the simulation of HOMO and LUMO illustrated in Fig. 9a-d present an overall similarity for the values of energy gap computed by Tauc's equation with a minor shift in values.

The Frontier molecular orbitals (FMO's) utilizing the generalized gradient approximation GGA/PW91method are recorded in Table 1. Figure 9a-d reveals the 3D HOMO and LUMO plots for [CMC], [TBA], [CMC + TBA]<sup>B</sup> and [CMC + TBA/CuO]<sup>C</sup> as- single crystal indicating the localization of EHOMO-EHOMO = 2.741 eV on the [CMC] and the energy [TBA] value is ELUMO-ELUMO = -2.671 eV). For [CMC + TBA]<sup>B</sup> and

[CMC + TBA/CuO]<sup>C</sup>, FMO's plots shows the localization of HOMO (-5.199 and -5.498 eV) on phenyl rings and that of LUMO (-2.610 and -3.299 eV) are spreading over the coordinated thiobarbituric acid and [CuO]<sup>NPs</sup>, respectively. The energy gap  $\Delta E = 2.199$  eV of [CMC + TBA/CuO]<sup>C</sup> nanocomposite is lower than that  $\Delta E = 2.589$  eV of [CMC + TBA]<sup>B</sup> bland which in turn shows that the present composites. These nanocomposite thin films are classified as suitable source for solar radiation processing in implementations for solar cells [56]. The electronegativity ( $\chi$ ) of [CMC + TBA]<sup>B</sup> (3.905 eV) acts as Lewis base while in case of [CMC + TBA/CuO]<sup>C</sup> (4.3985 eV) is extremely low value indicating a Lewis acid behavior. Table 3 provides data on chemical potential ( $\mu$ ), global hardness ( $\mu$ ), global softness's ( $\alpha$ ), global electrophilicity index ( $\omega$ ), maximum electronic loading ( $DN_{max}$ ) and softness ( $\sigma$ ) for calculating load transmission resistance and electron receivability in a molecule. It is clearly seen that [CMC + TBA/CuO]<sup>C</sup> with  $S = 0.4548$  eV,  $\omega = 8.7980$  eV,  $DN_{max} = 4.005$  and  $= 0.56$  eV<sup>-1</sup> value will be high soft than the [CMC], [TBA], [CMC + TBA]<sup>B</sup> [57].

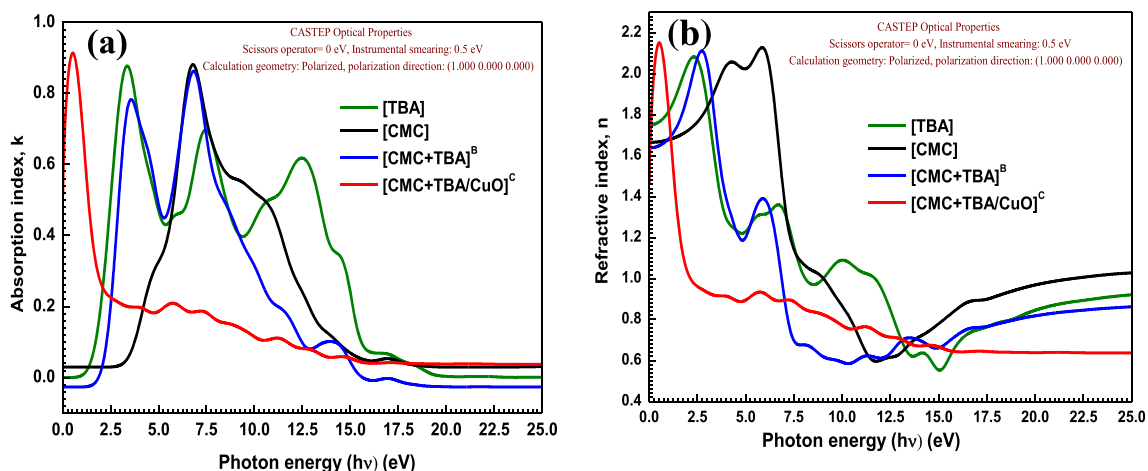


**Fig. 11** a The spectral dependence of the refractive index  $n(\lambda)$  with  $\lambda$  nm. b The absorption index  $k(\lambda)$  with  $\lambda$  nm for CMC, TBA<sup>F</sup>, [CMC + TBA]<sup>B</sup> and [CMC + TBA/CuO]<sup>C</sup> as - single crystal

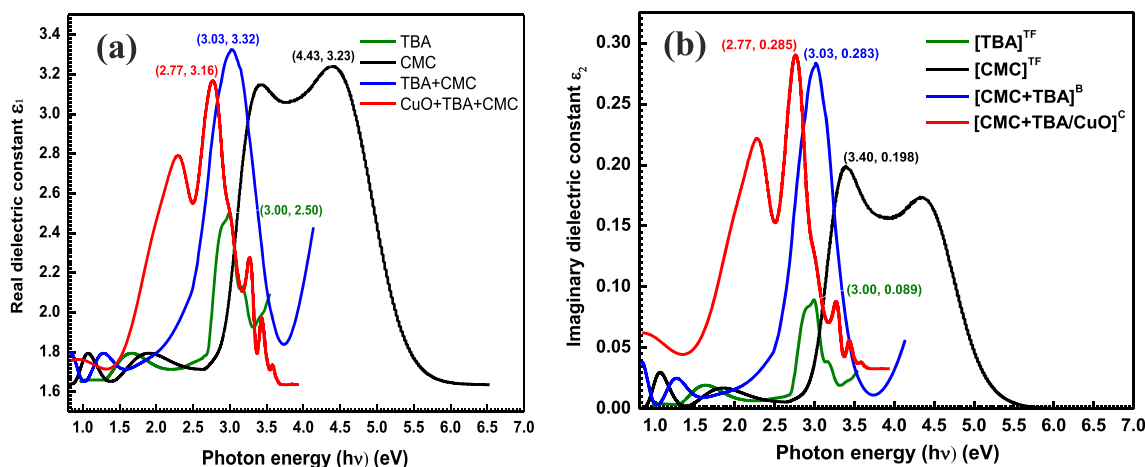


Fig. 12 a-b Experimental  $\epsilon_1$  and  $\epsilon_2$  via  $h\nu$  for  $[\text{CMC}]^{\text{TF}}$ ,  $[\text{TBA}]^{\text{TF}}$ ,  $[\text{CMC} + \text{TBA}]^{\text{B}}$  and  $[\text{CMC} + \text{TBA}/\text{CuO}]^{\text{C}}$

Polymers and inorganic compound are indeed very valuable for the development of nanomaterials and other equipment as solar cells. The absorption index  $k(\lambda)$  and refractive index  $n(\lambda)$  values, which included both absorption and refraction based on interference between the material examined and the light-incident.  $n(\lambda)$  has a phase velocity correlation with the dispersion, while  $k(\lambda)$  is linked to a mass reduction coefficient and permits the computation of the electromagnetic wave dissipation rate in medium. The spectroscopic reflectometry measurement of transmission and reflectance permits the  $n(\lambda)$  and  $k(\lambda)$  versus photon energy ( $h\nu$ ) to be defined. The spectral properties of  $n(\lambda)$  and  $k(\lambda)$  versus ( $h\nu$ ) values for  $[\text{CMC}]^{\text{TF}}$ ,  $[\text{TBA}]^{\text{TF}}$ ,  $[\text{CMC} + \text{TBA}]^{\text{B}}$  and  $[\text{CMC} + \text{TBA}/\text{CuO}]^{\text{C}}$  as-deposited thin film over a range 0.8–7 eV of ( $h\nu$ ) are given in Fig. 10a. Equation 1 is used to provide  $n(\lambda)$  and  $k(\lambda)$  values [58].

$$k(\lambda) = \frac{\alpha\lambda}{4\pi} \quad \text{and} \quad n(\lambda) = \sqrt{\frac{1+R}{1-R} - k^2} \quad (1)$$

For  $[\text{CMC}]^{\text{TF}}$ ,  $[\text{TBA}]^{\text{TF}}$ ,  $[\text{CMC} + \text{TBA}]^{\text{B}}$  and  $[\text{CMC} + \text{TBA}/\text{CuO}]^{\text{C}}$  as-deposited thin film in experimental section,  $n(\lambda)$  behavior showed the maximum peaks values at 1.79, 1.58, 1.83 and 1.78, respectively. Also, the peaks were also observed with  $k(\lambda)$ , with maximum values at 0.0559, 0.0282, 0.0777 and 0.0742 with a sudden fall at 4.5 eV, respectively. These peaks were linked to the  $\pi \rightarrow \pi^*$  benzenoid rings transition.

DFT calculation of  $[\text{CMC}]$ ,  $[\text{TBA}]$ ,  $[\text{CMC} + \text{TBA}]^{\text{B}}$  and  $[\text{CMC} + \text{TBA}/\text{CuO}]^{\text{C}}$  as-single crystal was utilized to predict  $n(\lambda)$  and  $k(\lambda)$  values (Fig. 11a-b). It is also important to note that the simulation curve illustrated in Fig. 11a-b present an overall similarity for  $n(\lambda)$  and  $k(\lambda)$  with a minor shift towards the highest energies with lower peak intensities.

The optical conductivity ( $\sigma$ ) and dielectric constants ( $\epsilon$ ) are the key elements for optical connections. The real dielectric constant ( $\epsilon_1$ ) and imaginary ( $\epsilon_2$ ) parts are computed as follows:  $\epsilon_1 = \epsilon_{\text{real}} = n^2 - k^2$ ,  $\epsilon_2 = \epsilon_{\text{img}} = 2nk$  and  $\omega = 2\pi f$  where  $\omega$  and  $f$  characterize the angular frequency and the applied frequency, respectively.  $\epsilon_1$  denote the material's ability to

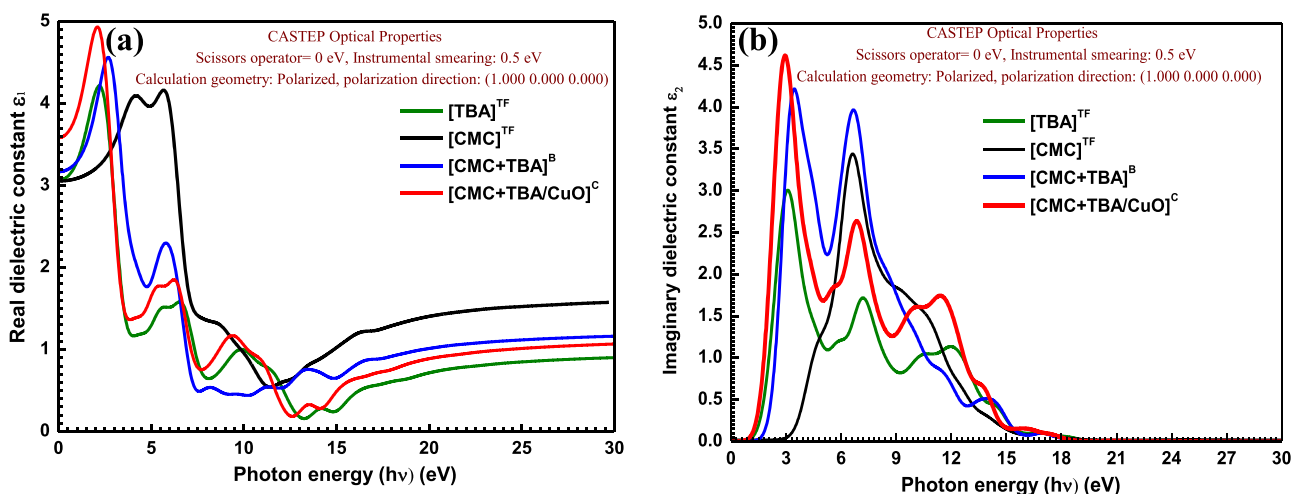
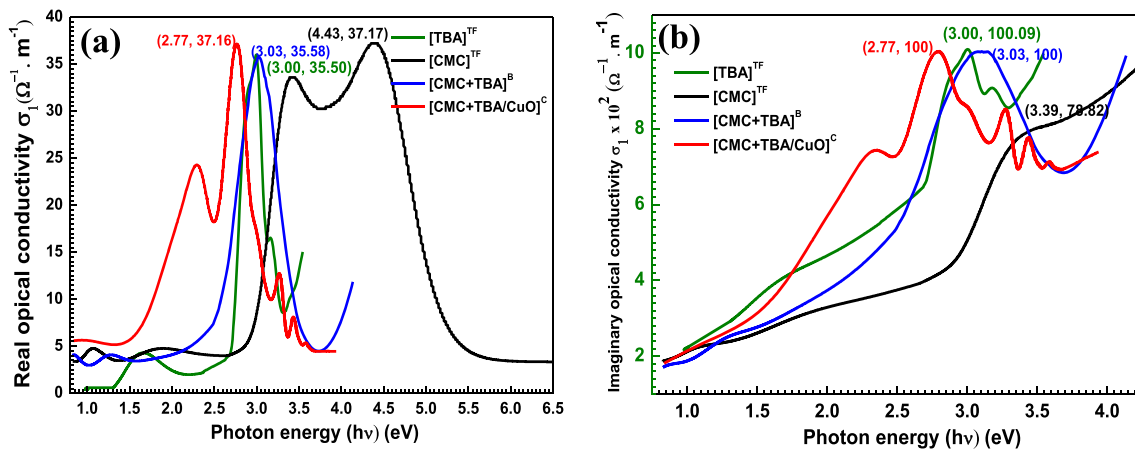


Fig. 13 a-b simulated  $\epsilon_1$  and  $\epsilon_2$  via  $h\nu$  for  $[\text{CMC}]$ ,  $[\text{TBA}]$ ,  $[\text{CMC} + \text{TBA}]^{\text{B}}$  and  $[\text{CMC} + \text{TBA}/\text{CuO}]^{\text{C}}$



**Fig. 14** a-b Experimental  $\sigma_1$  and  $\sigma_2$  via  $h\nu$  for  $[\text{CMC}]^{\text{TF}}$ ,  $[\text{TBA}]^{\text{TF}}$ ,  $[\text{CMC} + \text{TBA}]^{\text{B}}$  and  $[\text{CMC} + \text{TBA}/\text{CuO}]^{\text{C}}$

store electrical energy or to allow the electric field through it while  $\varepsilon_2$  is the material's loss and shows the material's ohmic resistance [59]. In experimental section (Fig. 12a-b), illustrate  $\varepsilon_1(\omega)$  and  $\varepsilon_2(\omega)$  vs  $h\nu$  behavior for  $[\text{CMC}]^{\text{TF}}$ ,  $[\text{TBA}]^{\text{TF}}$ ,  $[\text{CMC} + \text{TBA}]^{\text{B}}$  and  $[\text{CMC} + \text{TBA}/\text{CuO}]^{\text{C}}$  as-deposited thin film. The maximum real part  $\varepsilon_1(\omega)$  of  $[\text{CMC}]^{\text{TF}}$ ,  $[\text{TBA}]^{\text{TF}}$ ,  $[\text{CMC} + \text{TBA}]^{\text{B}}$  and  $[\text{CMC} + \text{TBA}/\text{CuO}]^{\text{C}}$  as-deposited thin film values are 3.23, 2.50, 3.32 and 2.77 at  $h\nu = 4.43, 3.00, 3.32$  and  $2.77$  eV, respectively. The imaginary part  $\varepsilon_2(\omega)$  displays the same behavior of  $\varepsilon_1(\omega)$  for  $[\text{CMC}]^{\text{TF}}$ ,  $[\text{TBA}]^{\text{TF}}$ ,  $[\text{CMC} + \text{TBA}]^{\text{B}}$  and  $[\text{CMC} + \text{TBA}/\text{CuO}]^{\text{C}}$  as-deposited thin film values are 0.198, 0.089, 0.283 and 0.285 at  $h\nu = 3.40, 3.00, 3.03$  and  $2.77$  eV, respectively. These results show that, the real part  $\varepsilon_1(\omega)$  of  $[\text{CMC}]^{\text{TF}}$ ,  $[\text{TBA}]^{\text{TF}}$ ,  $[\text{CMC} + \text{TBA}]^{\text{B}}$  and  $[\text{CMC} + \text{TBA}/\text{CuO}]^{\text{C}}$  as-deposited thin film are higher energy storage efficiency for the imaginary part  $\varepsilon_2(\omega)$ .

Figure 13(a-b) The spectral dependence of dielectric component versus photon energy ( $h\nu$ ) for  $[\text{CMC}]$ ,  $[\text{TBA}]$ ,  $[\text{CMC} + \text{TBA}]^{\text{B}}$  and  $[\text{CMC} + \text{TBA}/\text{CuO}]^{\text{C}}$  as-single by using DFT simulation. The simulation and experimental behavior of

dielectric constants is similar in behavior with different intensity of peaks and the photon energies ( $h\nu$ ) values

The optical conductivity  $\sigma(\omega)$  defines the optical response of the material as defined by the following expression. [60]:  $\sigma(\omega) = \sigma_1(\omega) + i\sigma_2(\omega)$ . The optical conductivity  $\sigma(\omega)$  is constituted by  $\sigma_1$  and  $\sigma_2$  which are the real and the imaginary parts, respectively. ( $\sigma_1$ ) and ( $\sigma_2$ ) are computed by the following equations: [61]:  $\sigma_1(\omega) = \omega\varepsilon_2\varepsilon_0$  and  $\sigma_2(\omega) = \omega\varepsilon_1\varepsilon_0$ , where  $\omega$  is the angular frequency,  $\varepsilon_0$  permittivity of free space. Figure 14a-b show optical conductivity variation of  $[\text{CMC}]^{\text{TF}}$ ,  $[\text{TBA}]^{\text{TF}}$ ,  $[\text{CMC} + \text{TBA}]^{\text{B}}$  and  $[\text{CMC} + \text{TBA}/\text{CuO}]^{\text{C}}$  vs  $h\nu$  and simulation using DFT of  $[\text{CMC}]$ ,  $[\text{TBA}]$ ,  $[\text{CMC} + \text{TBA}]^{\text{B}}$  and  $[\text{CMC} + \text{TBA}/\text{CuO}]^{\text{C}}$  (Fig. 15a-b). Compared to the experimental curve, the simulated curve for each compound clearly demonstrate good compliance. Both real part ( $\sigma_1$ ) and the imaginary part ( $\sigma_2$ ) corresponding to  $[\text{CMC}]^{\text{TF}}$ ,  $[\text{TBA}]^{\text{TF}}$ ,  $[\text{CMC} + \text{TBA}]^{\text{B}}$  and  $[\text{CMC} + \text{TBA}/\text{CuO}]^{\text{C}}$  increased with photon energy increases until arrived 3.80 eV. The behavior of optical conductivity can be assigned to the electron's excitation. The real conductivity ( $\sigma_1$ ) for  $[\text{CMC}]^{\text{TF}}$ ,  $[\text{TBA}]^{\text{TF}}$ ,  $[\text{CMC} + \text{TBA}]^{\text{B}}$  and  $[\text{CMC} +$

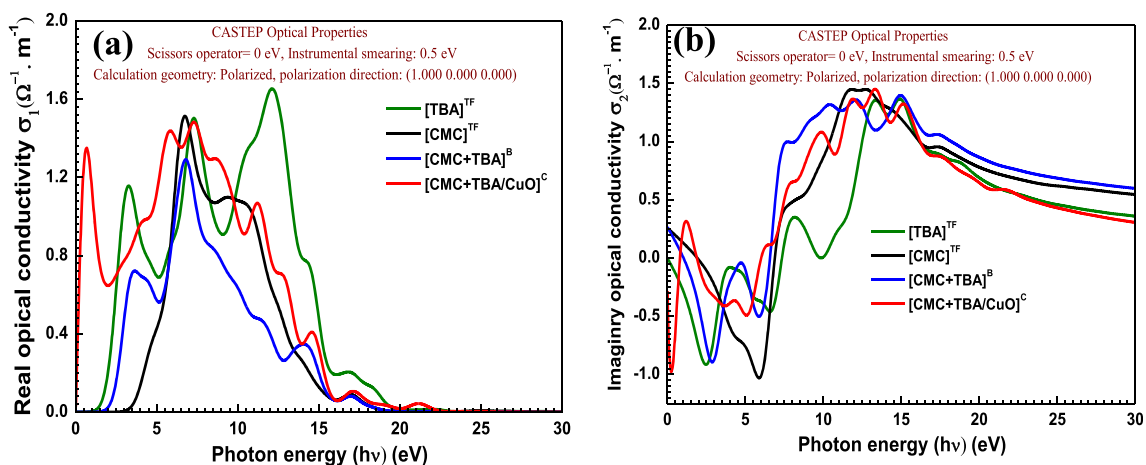
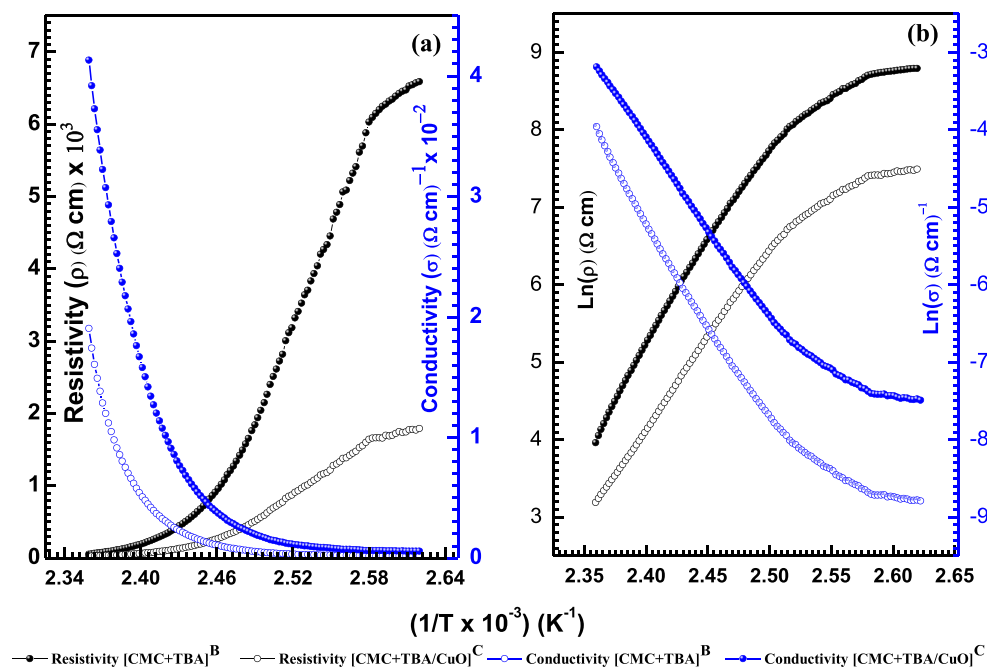


**Fig. 15** a-b  $\sigma_1$  and  $\sigma_2$  simulation optical properties for  $[\text{CMC}]$ ,  $[\text{TBA}]$ ,  $[\text{CMC} + \text{TBA}]^{\text{B}}$  and  $[\text{CMC} + \text{TBA}/\text{CuO}]^{\text{C}}$  by using CASTEP method in DFT



**Fig. 16 a-b** Plot of  $\rho$  and  $\text{Ln}\sigma$  versus  $1/T$  of  $[\text{CMC} + \text{TBA}]^{\text{B}}$  and  $[\text{CMC} + \text{TBA}/\text{CuO}]^{\text{C}}$  as-deposited thin films



$[\text{CMC} + \text{TBA}/\text{CuO}]^{\text{C}}$  have one distinct signals of  $(37.17 \Omega^{-1} \text{ m}^{-1}$  at 4.43 eV),  $(35.50 \Omega^{-1} \text{ m}^{-1}$  at 3.00 eV),  $(35.58 \Omega^{-1} \text{ m}^{-1}$  at 3.03 eV) and  $(37.16 \Omega^{-1} \text{ m}^{-1}$  at 2.77 eV), respectively. The optical conductivity increases of  $[\text{CMC}]^{\text{TF}}$ ,  $[\text{TBA}]^{\text{TF}}$ ,  $[\text{CMC} + \text{TBA}]^{\text{B}}$  and  $[\text{CMC} + \text{TBA}/\text{CuO}]^{\text{C}}$  which is possibly attributed to the coefficient of high absorbance related to charge ordering effect. The optical conductivity and absorption coefficient are linked by the following equation [62]:  $\sigma = \alpha nc/4\pi$  Considering that  $c$  is the light speed,  $\alpha$  is the refractive index and  $n$  the coefficient of absorption. The real conductivity ( $\sigma_2$ ) for  $[\text{CMC}]^{\text{TF}}$ ,  $[\text{TBA}]^{\text{TF}}$ ,  $[\text{CMC} + \text{TBA}]^{\text{B}}$  and  $[\text{CMC} + \text{TBA}/\text{CuO}]^{\text{C}}$  have one distinct signals of  $(78.82 \Omega^{-1} \text{ m}^{-1}$  at 3.39 eV),  $(100.09 \Omega^{-1} \text{ m}^{-1}$  at 3.00 eV),  $(100 \Omega^{-1} \text{ m}^{-1}$  at 3.03 eV) and  $(100 \Omega^{-1} \text{ m}^{-1}$  at 2.77 eV), respectively.

Figure 15 a-b The spectral dependence of optical conductivity  $\sigma(\omega)$  versus photon energy ( $h\nu$ ) for  $[\text{CMC}]$ ,  $[\text{TBA}]$ ,  $[\text{CMC} + \text{TBA}]^{\text{B}}$  and  $[\text{CMC} + \text{TBA}/\text{CuO}]^{\text{C}}$  as-single by using DFT simulation. The simulation and experimental behavior of optical conductivity  $\sigma(\omega)$  is similar in behavior with different intensity of peaks and the photon energies ( $h\nu$ ) values.

**Electrical properties (direct current (DC) conductivity) of  $[\text{CMC} + \text{TBA}]^{\text{B}}$  and  $[\text{CMC} + \text{TBA}/\text{CuO}]^{\text{C}}$  thin film**

Conductivity study is one of the most interesting instruments to characterize  $[\text{CMC} + \text{TBA}]^{\text{B}}$  and  $[\text{CMC} + \text{TBA}/\text{CuO}]^{\text{C}}$  as-deposited thin films. The 4-probe van der Pauw methodology was used for calculating DC conductivities. Electric conductivity of the  $[\text{CMC} + \text{TBA}]^{\text{B}}$  and  $[\text{CMC} + \text{TBA}/\text{CuO}]^{\text{C}}$  as-deposited thin films at room temperature was found to be  $3.56 \times 10^{-2} (\Omega \text{ cm})^{-1}$  and  $8.05 \times 10^{-2} (\Omega \text{ cm})^{-1}$ , respectively. The conductivity of the  $[\text{CMC} + \text{TBA}]^{\text{B}}$  and  $[\text{CMC} + \text{TBA}/\text{CuO}]^{\text{C}}$  as-deposited thin films increases with increasing of the temperature attributed to the rise of charge transfer efficacy [63]. In addition, the curling of the blend and composites thin films chain attribute to thermal transfer has been proposed. This phenomenon increases the conjugation within the  $[\text{CMC} + \text{TBA}]^{\text{B}}$  and  $[\text{CMC} + \text{TBA}/\text{CuO}]^{\text{C}}$  backbone and enhances its electric conductivity [64]. The electrical conductivity of the  $[\text{CMC} + \text{TBA}]^{\text{B}}$  and  $[\text{CMC} + \text{TBA}/\text{CuO}]^{\text{C}}$  as-deposited thin films ranged from 298 K to 400 K.

**Table 4** The activation energy of  $[\text{CMC} + \text{TBA}]^{\text{B}}$  and  $[\text{CMC} + \text{TBA}/\text{CuO}]^{\text{C}}$

Compound	$\Delta E$ by DFT (eV)	$\Delta E$ by Tauc equation (eV)	$\Delta E$ by DC (eV)	Refs
[CMC]	–	–	2.76	[67]
[CMC/TiO <sub>2</sub> (1%)]	–	–	2.68	[67]
[SiC/SiO <sub>2</sub> + CMC]	–	–	6.415	[68]
$[\text{CMC} + \text{TBA}]^{\text{B}}$	2.589	2.629	2.79	Present work
$[\text{CMC} + \text{TBA}/\text{CuO}]^{\text{C}}$	2.199	2.488	2.03	Present work

The plot  $\ln(\rho)$  versus  $1/T$  for  $[\text{CMC} + \text{TBA}]^{\text{B}}$  and  $[\text{CMC} + \text{TBA}/\text{CuO}]^{\text{C}}$  as shown in the Fig. 16(a–b). Constructed on the relationship between plot  $\ln(\rho)$  versus  $1/T$ , the  $E_a$  computed from the following equation [65]:

$$\rho = \rho_0 \exp^{E_a/KT},$$

where  $\rho_0$  a constant,  $K$  is the Boltzmann constant,  $T$  is the temperature in Kelvin and  $E_a$  is activation energy. The resistivity and the conductivity of  $[\text{CMC} + \text{TBA}]^{\text{B}}$  and  $[\text{CMC} + \text{TBA}/\text{CuO}]^{\text{C}}$  strongly depend on the temperature.

It is detected that in the temperature ranges considered [(399–423 K (region I) and (399–381 K (region II)], the  $[\text{CMC} + \text{TBA}]^{\text{B}}$  as-deposited thin films exhibits two activation energies are  $E_{a1} = 2.279$  eV for the region I and  $E_{a2} = 0.947$  eV for the region II. While, the  $[\text{CMC} + \text{TBA}/\text{CuO}]^{\text{C}}$  as-deposited thin films exhibits two activation energies are  $E_{a1} = 2.03$  eV for the region I and  $E_{a2} = 0.939$  eV for the region II. The first activation energy ( $E_{a1}$ ) is generated at a high temperature, the  $[\text{CMC} + \text{TBA}]^{\text{B}}$  and  $[\text{CMC} + \text{TBA}/\text{CuO}]^{\text{C}}$  thin films electrical conductivity is caused by thermal excitation of charge transfers from grain boundaries to neutral areas [66]. The second energy activation ( $E_{a2}$ ) is significantly smaller than ( $E_{a1}$ ) for the region of the lower temperature. The dimension of conductivity may also have been caused by transport (hopping) of the carriers to localized countries in the region near the  $[\text{CMC} + \text{TBA}]^{\text{B}}$  and  $[\text{CMC} + \text{TBA}/\text{CuO}]^{\text{C}}$  thin film conductivity band. Activation energy computed by the optical characteristics at high temperature region ( $E_{a1}$ ).

Table 4 illustrates a significant difference between the activation energy values published in this study for  $[\text{CMC} + \text{TBA}]^{\text{B}}$  and  $[\text{CMC} + \text{TBA}/\text{CuO}]^{\text{C}}$  and that reported previously in literature. It can be attributed to the various materials used in each study and the formation of a crystalline or amorphous CMC nanocomposite. The activation energy determined by this study is significantly smaller than those published previously showing that the  $[\text{TBA}]$  and  $[\text{CuO}]^{\text{NPs}}$  blends are more susceptible to oxidation in air compared to  $[\text{TiO}_2]^{\text{NPs}}$ . This can be attributed to the fabrication of a smooth and dense  $[\text{CMC} + \text{TBA} / \text{CuO}]^{\text{C}}$  nanocomposite film and it was confirmed by AFM study.

## Conclusion

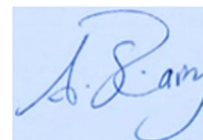
$[\text{CMC}]^{\text{TF}}$ ,  $[\text{TBA}]^{\text{TF}}$ ,  $[\text{CMC} + \text{TBA}]^{\text{B}}$  and  $[\text{CMC} + \text{TBA}/\text{CuO}]^{\text{C}}$  as-deposited thin films are fabricated with significant

structural characteristics, optical dispersion and dielectric properties. Studies in XRD revealed that the same crystal structure was observed for  $[\text{CuO}]^{\text{NPs}}$  and  $[\text{CMC} + \text{TBA}/\text{CuO}]^{\text{C}}$  (Triclinic) with space group ( $P\bar{1}$ ). In addition,  $[\text{CuO}]^{\text{NPs}}$  grain size ( $D$  size = 25.479 nm) was found to be smaller than  $[\text{CMC} + \text{TBA}/\text{CuO}]^{\text{C}}$  ( $D$  size = 28.09 nm). The  $E_g^{\text{Opt}}$  values obtained from Tauc's equation are 2.978 eV, 2.725 eV, 2.625 eV and 2.488 eV for  $[\text{CMC}]^{\text{TF}}$ ,  $[\text{TBA}]^{\text{TF}}$ ,  $[\text{CMC} + \text{TBA}]^{\text{B}}$  and  $[\text{CMC} + \text{TBA}/\text{CuO}]^{\text{C}}$  as-deposited thin films, respectively. While the  $E_g^{\text{Opt}}$  computed by DFT ( $\text{DMol}^3$ ) are 2.741 eV, 2.671 eV, 2.589 eV and 2.199 eV for  $[\text{CMC}]^{\text{TF}}$ ,  $[\text{TBA}]^{\text{TF}}$ ,  $[\text{CMC} + \text{TBA}]^{\text{B}}$  and  $[\text{CMC} + \text{TBA}/\text{CuO}]^{\text{C}}$  as-deposited thin films, respectively. There is a good agreement between them in accordance with the  $E_g^{\text{Opt}}$  values determined by DFT ( $\text{DMol}^3$ ) computations with the Tauc's equation. The refractive index  $n$ , absorption index ( $k$ ) and optical conductivity were enhanced with increased photon energy. The simulated FTIR (*Gaussian DFT*), XRD (*precited PMP*), and optical properties (*CATSTEP*) of  $[\text{CMC} + \text{TBA}]^{\text{B}}$  and  $[\text{CMC} + \text{TBA}/\text{CuO}]^{\text{C}}$  in isolated and gas state are in great compliance for both  $[\text{CMC} + \text{TBA}]^{\text{B}}$  and  $[\text{CMC} + \text{TBA}/\text{CuO}]^{\text{C}}$  as-deposited thin films experimental analyses. The optical constants, refractive indicator ( $n$ ), absorption index ( $k$ ) and optical conductivity increase with increased photon energies ( $h\nu$ ). For increased photon energy the optical constants; refractive index  $n$ , absorption index  $k$ , and optical conductivity are increasing. The results of the optical characteristics confirm a  $[\text{CMC} + \text{TBA}/\text{CuO}]^{\text{C}}$  as-deposited thin films constructed heterojunction can be utilized as a solar cell and transistors and these properties are improved by formation of nanocomposite. The electrical conductivities of the both  $[\text{CMC} + \text{TBA}]^{\text{B}}$  and  $[\text{CMC} + \text{TBA}/\text{CuO}]^{\text{C}}$  as-deposited thin films were found to be  $3.56 \times 10^{-2} (\Omega \text{ cm})^{-1}$  and  $8.05 \times 10^{-2} (\Omega \text{ cm})^{-1}$  at room temperature, respectively. Based on the optical conductivity, dielectric constants, particle size, AFM studies, activation energy by DC ( $E_{a1}$ ), DFT calculation ( $E_H - E_L$ ) and band gap ( $E_g^{\text{Opt}}$ ) of  $[\text{CMC} + \text{TBA}]^{\text{B}}$  and  $[\text{CMC} + \text{TBA}/\text{CuO}]^{\text{C}}$  nanocomposite films can be used as optoelectronic device.

## Compliance with ethical standards

**Declaration of interests** The authors declare that they have no known competing financial interests or personal relationships that could have appeared to influence the work reported in this paper.

The authors declare the following financial interests/personal relationships which may be considered as potential competing interests:



Prof. Ahmed F. Al-Hossainy

## References

- Qi X-D, Wang Y (2020) Novel techniques for the preparation of shape-memory polymers, Polymer Blends and Composites at Micro and Nanoscales, Shape Memory Polymers, Blends and Composites, Springer, pp. 53–83
- Zarrintaj P, Saeb MR, Jafari SH, Mozafari M (2020) Application of compatibilized polymer blends in biomedical fields, Compatibilization of Polymer Blends, Elsevier, pp. 511–537
- Correa A, Pereira E, de Oliveira A (2020) Magnetic properties of conducting polymers, Emerging Research in Science and Engineering Based on Advanced Experimental and Computational Strategies, Springer, pp. 493–510
- Abd-Elmageed A, Al-Hossainy A, Fawzy E, Almutlaq N, Eid M, Bourezgui A, Abdel-Hamid S, Elsharkawy N, Zwawi M, Abdel-Aziz M (2020) Synthesis, characterization and DFT molecular modeling of doped poly (Para-nitroaniline-co-Para-toluidine) thin film for optoelectronic devices applications. *Opt Mater* 99:109593
- El Sayed A, El-Gamal S (2015) Synthesis and investigation of the electrical and dielectric properties of co 3 O 4/(CMC+ PVA) nanocomposite films. *J Polym Res* 22:97
- Wu D, Chang PR, Ma X (2011) Preparation and properties of layered double hydroxide–carboxymethylcellulose sodium/glycerol plasticized starch nanocomposites. *Carbohydr Polym* 86:877–882
- Singh BK, Dutta PK (2016) Chitin, chitosan, and silk fibroin electrospun nanofibrous scaffolds: a prospective approach for regenerative medicine, Chitin and Chitosan for Regenerative Medicine, Springer, pp. 151–189
- Wang Y, Zhang Z, Wang M, Guo C, Liu H, Zeng H, Duan X, Zhou Y, Tang Z (2018) Direct electrodeposition of carboxymethyl cellulose based on coordination deposition method. *Cellulose* 25:105–115
- Hamer JW (1995) [Method of processing] photographic elements having fogged grains and development inhibitors for interimage, Google Patents 5:399,466
- Bourezgui A, Kacem I, Daoudi M, Al-Hossainy AF (2020) Influence of gamma-irradiation on structural, optical and Photocatalytic performance of TiO<sub>2</sub> nanoparticles under controlled atmospheres. *J Electron Mater* 49:1904–1921
- Costa H, Gallego SM, Tomaro MAL (2002) Effect of UV-B radiation on antioxidant defense system in sunflower cotyledons. *Plant Sci* 162:939–945
- Venil CK, Zakaria ZA, Ahmad WA (2013) Bacterial pigments and their applications. *Process Biochem* 48:1065–1079
- Islam S, Bhuiyan MR, Islam M (2017) Chitin and chitosan: structure, properties and applications in biomedical engineering. *J Polym Environ* 25:854–866
- Agarwal R, Alam MS, Gupta B (2013) Polyvinyl alcohol-polyethylene oxide-carboxymethyl cellulose membranes for drug delivery. *J Appl Polym Sci* 129:3728–3736
- Youssef AM, El-Sayed SM, El-Sayed HS, Salama HH, Dufresne A (2016) Enhancement of Egyptian soft white cheese shelf life using a novel chitosan/carboxymethyl cellulose/zinc oxide bionanocomposite film. *Carbohydr Polym* 151:9–19
- Esmailzadeh P, Hosseinpour N, Bahramian A, Fakhrouiean Z, Arya S (2014) Effect of ZrO<sub>2</sub> nanoparticles on the interfacial behavior of surfactant solutions at air–water and n-heptane–water interfaces. *Fluid Phase Equilib* 361:289–295
- Babu IM, William JJ, Muralidharan G (2019) Ordered mesoporous Co<sub>3</sub>O<sub>4</sub>/CMC nanoflakes for superior cyclic life and ultra high energy density supercapacitor. *Appl Surf Sci* 480:371–383
- Yadav M, Rhee KY, Park S (2014) Synthesis and characterization of graphene oxide/carboxymethylcellulose/alginate composite blend films. *Carbohydr Polym* 110:18–25
- Yang Z, Zhao W, Niu Y, Zhang Y, Wang L, Zhang W, Xiang X, Li Q (2018) Direct spinning of high-performance graphene fiber supercapacitor with a three-ply core-sheath structure. *Carbon* 132: 241–248
- Alizadegan R, Liao AD, Xiong F, Pop E, Hsia KJ (2012) Effects of tip-nanotube interactions on atomic force microscopy imaging of carbon nanotubes. *Nano Res* 5:235–247
- Yun Y (2006) Nanotube sensors and actuators in mechanics and medicine, University of Cincinnati
- Ibrahim E, Abdel-Rahman LH, Abu-Dief AM, Elshafaie A, Hamdan SK, Ahmed A (2018) The synthesis of CuO and NiO nanoparticles by facile thermal decomposition of metal-Schiff base complexes and an examination of their electric, thermoelectric and magnetic properties. *Mater Res Bull* 107:492–497
- Wu R, Qian X, Yu F, Liu H, Zhou K, Wei J, Huang Y (2013) MOF-templated formation of porous CuO hollow octahedra for lithium-ion battery anode materials. *J Mater Chem A* 1:11126–11129
- Alizadeh-Gheshlaghi E, Shaabani B, Khodayari A, Azizian-Kalandaragh Y, Rahimi R (2012) Investigation of the catalytic activity of nano-sized CuO, Co<sub>3</sub>O<sub>4</sub> and CuCo<sub>2</sub>O<sub>4</sub> powders on thermal decomposition of ammonium perchlorate. *Powder Technol* 217:330–339
- Abdel-Aziz M, Zoromba MS, Bassyouni M, Zwawi M, Alshehri A, Al-Hossainy A (2020) Synthesis and characterization of co-Al mixed oxide nanoparticles via thermal decomposition route of layered double hydroxide, *J Molec Struct*, 127679
- Zoromba MS, Al-Hossainy A (2020) Doped poly (o-phenylenediamine-co-p-toluidine) fibers for polymer solar cells applications. *Sol Energy* 195:194–209
- Akash MSH, Rehman K (2020) Infrared spectroscopy, Essentials of Pharmaceutical Analysis, Springer, pp. 57–80
- Al-Hossainy AF, Eid MR, Zoromba MS (2019) Prediction of molecular characteristics and molecular spectroscopy of hydrochloric acid-doped poly (ortho-Anthranilic acid-co-Para Nitroaniline) thin film. *J Electron Mater* 48:8107–8115
- Paul D, Neogi S (2019) Synthesis, characterization and a comparative antibacterial study of CuO, NiO and CuO-NiO mixed metal oxide. *Mater Res Exp* 6:055004
- Hassan FS, Al-Hossainy AF, Mohamed AE (2009) Diphosphine compounds, part III: UV/visible spectroscopy and novel routes to functionalized diphosphine-M (CO) 6 complexes (M= W, Mo, or Cr). *Phosphorus Sulfur Silicon* 184:2996–3022
- Minami N, Kim Y, Miyashita K, Kazaoui S, Nalini B (2006) Cellulose derivatives as excellent dispersants for single-wall carbon nanotubes as demonstrated by absorption and photoluminescence spectroscopy. *Appl Phys Lett* 88:093123
- Hebeish A, Sharaf S (2015) Novel nanocomposite hydrogel for wound dressing and other medical applications. *RSC Adv* 5: 103036–103046
- Al-Hossainy AF, Zoromba MS (2019) Doped-poly (Para-nitroaniline-co-aniline): synthesis, semiconductor characteristics, density, functional theory and photoelectric properties. *J Alloys Compd* 789:670–683
- Zohuriaan M, Shokrolahi F (2004) Thermal studies on natural and modified gums. *Polym Test* 23:575–579
- Zoromba MS, Bassyouni M, Abdel-Aziz M, Al-Hossainy AF, Salah N, Al-Ghamdi A, Eid MR (2019) Structure and photoluminescence characteristics of mixed nickel–chromium oxides nanostructures. *Applied Physics A* 125:642
- Jäger N, Meindlumer M, Spor S, Hrubi H, Julin J, Stark A, Nahif F, Keckes J, Mitterer C, Daniel R (2020) Microstructural evolution and thermal stability of AlCr (Si) N hard coatings revealed by in-situ high-temperature high-energy grazing incidence transmission X-ray diffraction. *Acta Mater* 186:545–554
- Al-Hossainy AF, Eid MR, Zoromba MS (2019) Structural, DFT, optical dispersion characteristics of novel [DPPA-Zn-MR

- (cl)(H<sub>2</sub>O)] nanostructured thin films. *Mater Chem Phys* 232:180–192
38. Bzik S, Jansen M (2003) X-ray diffraction studies on Mesophases of Cetyl-and Dodecyltrimethylammoniumbromide in liquid Ammonia. *Chem Eur J* 9:613–620
  39. Roy A (2018) Hybrid Polyaniline Nanocomposite For Humidity Sensing, Lulu.com
  40. Abdel-Aziz M, Al-Hossainy A, Ibrahim A, El-Maksoud SA, Zoromba MS, Bassyouni M, Abdel-Hamid S, Abd-Elmageed A, Elsayed I, Alqahtani O (2018) Synthesis, characterization and optical properties of multi-walled carbon nanotubes/aniline-o-anthranilic acid copolymer nanocomposite thin films. *J Mater Sci Mater Electron* 29:16702–16714
  41. Al-Hossainy A, Thabet HK, Zoromba MS, Ibrahim A (2018) Facile synthesis and fabrication of a poly (ortho-anthranilic acid) emeraldine salt thin film for solar cell applications. *New J Chem* 42:10386–10395
  42. Starova G, Krivovichev S, Filatov S (1998) Crystal chemistry of inorganic compounds based on chains of oxocentered tetrahedra. II. Crystal structure of Cu<sub>4</sub>O<sub>2</sub> [(As, V) O<sub>4</sub>] Cl<sub>11</sub>. *Z Krist* 213:650–653
  43. Duman F, Ocoy I, Kup FO (2016) Chamomile flower extract-directed CuO nanoparticle formation for its antioxidant and DNA cleavage properties. *Mater Sci Eng C* 60:333–338
  44. El Sayed A, El-Gamal S, Morsi W, Mohammed G (2015) Effect of PVA and copper oxide nanoparticles on the structural, optical, and electrical properties of carboxymethyl cellulose films. *J Mater Sci* 50:4717–4728
  45. Al-Hossainy A, Bassyouni M, Zoromba MS (2018) Elucidation of electrical and optical parameters of poly (o-anthranilic acid)-poly (o-amino phenol)/copper oxide nanocomposites thin films. *J Inorg Organomet Polym Mater* 28:2572–2583
  46. Yao H, Qian D, Zhang H, Qin Y, Xu B, Cui Y, Yu R, Gao F, Hou J (2018) Critical role of molecular electrostatic potential on charge generation in organic solar cells. *Chin J Chem* 36:491–494
  47. El-Gammal OA, Al-Hossainy AF, El-Brashy SA (2018) Spectroscopic, DFT, optical band gap, powder X-ray diffraction and bleomycin-dependant DNA studies of co (II), Ni (II) and cu (II) complexes derived from macrocyclic Schiff base. *J Mol Struct* 1165:177–195
  48. Saadiah M, Zhang D, Nagao Y, Muzakir S, Samsudin A (2019) Reducing crystallinity on thin film based CMC/PVA hybrid polymer for application as a host in polymer electrolytes. *J Non-Cryst Solids* 511:201–211
  49. Al-Hossainy A, Zoromba MS (2018) New organic semiconductor thin film derived from p-toluidine monomer. *J Mol Struct* 1156:83–90
  50. Kumar TA, Mariselvi P, Alagumuthu G (2019) Optical and Photocatalytic activity of Cmc capped zinc Selenide nanoparticles under UV light irradiation using Congo red dye. *J Catalyst Catalysis* 6:25–35
  51. Al-Hossainy A, Zoromba MS, El-Gammal O, El-Dossoki FI (2019) Density functional theory for investigation of optical and spectroscopic properties of zinc-quinonoid complexes as semiconductor materials. *Struct Chem* 30:1365–1380
  52. Polak MP, Kudrawiec R, Rubel O (2019) Electronic band structure of nitrogen diluted Ga (PAsN): formation of the intermediate band, direct and indirect optical transitions, and localization of states. *J Appl Phys* 126:175701
  53. Al-Hossainy A, Zoromba MS, Abdel-Aziz M, Bassyouni M, Attar A, Zwawi M, Abd-Elmageed A, Maddah H, Slimane AB (2019) Fabrication of heterojunction diode using doped-poly (ortho-aminophenol) for solar cells applications. *Phys B Condens Matter* 566:6–16
  54. Badry R, El-Khodary S, Elhaes H, Nada N, Ibrahim M (2019) The influence of moisture on the electronic properties of monomer, dimer, Trimer and Emeraldine Base sodium Carboxymethyl cellulose. *Egypt J Chem* 62:39–56
  55. Zoromba MS, Abdel-Aziz M, Bassyouni M, Bahaitham H, Al-Hossainy A (2018) Poly (o-phenylenediamine) thin film for organic solar cell applications. *J Solid State Electrochem* 22:3673–3687
  56. De La Mora M, Amelines-Sarria O, Monroy B, Hernández-Pérez C, Lugo J (2017) Materials for downconversion in solar cells: perspectives and challenges. *Sol Energy Mater Sol Cells* 165:59–71
  57. Yousefi A, Aslanzadeh SA, Akbari J (2018) Experimental and DFT studies of 1-methylimidazolium trinitrophenoxide as modifier for corrosion inhibition of SDS for mild steel in hydrochloric acid. *Anti-Corrosion Methods and Materials* 65:107–122
  58. Sørensen KT, Ingvorsen CB, Nielsen LH, Kristensen A (2018) Effects of water-absorption and thermal drift on a polymeric photonic crystal slab sensor. *Opt Express* 26:5416–5422
  59. Hashim A, Hadi Q (2018) Structural, electrical and optical properties of (biopolymer blend/titanium carbide) nanocomposites for low cost humidity sensors. *J Mater Sci Mater Electron* 29:11598–11604
  60. Ibrahim A, Abdel-Aziz M, Zoromba MS, Al-Hossainy A (2018) Structural, optical, and electrical properties of multi-walled carbon nanotubes/polyaniline/Fe<sub>3</sub>O<sub>4</sub> ternary nanocomposites thin film. *Synth Met* 238:1–13
  61. Al-Hossainy AF, Abd-Elmageed A, Ibrahim ATA (2015) Synthesis, structural and optical properties of gold nanoparticle-graphene-selenocysteine composite bismuth ultrathin film electrode and its application to Pb (II) and Cd (II) determination. *Arab J Chemist*
  62. Habeeb MA, Hashim A, Hadi A (2017) Fabrication of new nanocomposites: CMC-PAA-PbO<sub>2</sub> nanoparticles for piezoelectric sensors and gamma radiation shielding applications. *Sens Lett* 15:785–790
  63. Kuo S-Y, Chen W-C, Lai F-I, Cheng C-P, Kuo H-C, Wang S-C, Hsieh W-F (2006) Effects of doping concentration and annealing temperature on properties of highly-oriented Al-doped ZnO films. *J Cryst Growth* 287:78–84
  64. Zoromba MS, Al-Hossainy A, Abdel-Aziz M (2017) Conductive thin films based on poly (aniline-co-o-anthranilic acid)/magnetite nanocomposite for photovoltaic applications. *Synth Met* 231:34–43
  65. Raja V, Sharma A, Rao VN (2004) Impedance spectroscopic and dielectric analysis of PMMA-CO-P4VPNO polymer films. *Mater Lett* 58:3242–3247
  66. Ma T, Liu Z, Wen J, Gao Y, Ren X, Chen H, Jin C, Ma X-L, Xu N, Cheng H-M (2017) Tailoring the thermal and electrical transport properties of graphene films by grain size engineering. *Nat Commun* 8:1–9
  67. Abdel-Galil A, Ali H, Atta A, Balboul M (2014) Influence of nanostructured TiO<sub>2</sub> additives on some physical characteristics of carboxymethyl cellulose (CMC). *J Radiat Res Appl Sci* 7:36–43
  68. Al Nasiri N, Patra N, Ni N, Jayaseelan DD, Lee WE (2016) Oxidation behaviour of SiC/SiC ceramic matrix composites in air. *J Eur Ceram Soc* 36:3293–3302

**Publisher's note** Springer Nature remains neutral with regard to jurisdictional claims in published maps and institutional affiliations.